From the Sun to the Earth: August 25, 2018 geomagnetic storm effects

Mirko Piersanti[1], Paola De Michelis[2], Dario Del Moro[3], Roberta Tozzi[2], Michael Pezzopane[2], Giuseppe Consolini[4], Maria Federica Marcucci[4], Monica Laurenza[4], Simone Di Matteo[5], Alessio Pignalberi[2], Virgilio Quattrociocchi[4,6], and Piero Diego[4]

[1]INFN - University of Rome "Tor Vergata", Rome, Italy.
[2]Istituto Nazionale di Geofisica e Vulcanologia, Rome, Italy.
[3]University of Rome "Tor Vergata", Rome, Italy.
[4]INAF-Istituto di Astrofisica e Planetologia Spaziali, Rome, Italy.
[5]Catholic University of America at NASA Goddard Space Flight Center, Greenbelt, Maryland, USA
[6]Dpt. of Physical and Chemical Sciences, University of L'Aquila, L'Aquila, Italy

Correspondence: Mirko Piersanti (mirko.piersanti@roma2.infn.it)

Abstract. On August 25, 2018 the interplanetary counterpart of the August 20, 2018 Coronal Mass Ejection (CME) hit the Earth, giving rise to a strong G3 geomagnetic storm. We present a description of the whole sequence of events from the Sun to the ground as well as a detailed analysis of the observed effects on the Earth's environment by using a multi instrumental approach. We studied the ICME propagation in the interplanetary space up to the analysis of its effects in the magnetosphere, ionosphere and at ground. To accomplish this task, we used ground and space collected data, including data from CSES (China Seismo Electric Satellite), launched on February 11, 2018. We found a direct connection between the ICME impact point onto the magnetopause and the pattern of the Earth's auroral electrojects. Using the Tsyganenko TS04 model prevision, we were able to correctly identify the principal magnetospheric current system activating during the different phases of the geomagnetic storm. Moreover, we analyzed the space-weather effects associated with the August 25, 2018 solar event in terms of evaluation geomagnetically induced currents (GIC) and identification of possible GPS loss of lock. We found that, despite the strong geomagnetic storm, no loss of lock has been detected. On the contrary, the GIC hazard was found to be potentially more dangerous than other past, more powerful solar events, such as the 2015 St. Patrick geomagnetic storm, especially at latitudes higher than $60°$ in the European sector.

1 Introduction

Geomagnetic storms and substorms are among the most important signatures of the variability in the solar-terrestrial relationships. They are extremely complicated processes, which are triggered by the arrival of solar perturbations, such as coronal mass ejections (CMEs), solar flares, corotating interaction regions and so on (e.g. *Gosling*, 1993; *Bothmer and Schwenn*, 1995; *Gon-*

zales and Tsurutani, 1987; *Piersanti et al.*, 2017), and affect the entire magnetosphere. Indeed, these processes are both highly
non linear and multiscale, involving a wide range of plasma regions and phenomena in both the magnetosphere and ionosphere
that mutually interact. Computer simulations, ground-based and space-borne observations, over the last thirty years, have high-
lighted such strong feedback and coupling processes (*Piersanti et al.*, 2017, and references therein). This is the reason why,
to properly understand geomagnetic storms and magnetospheric substorms, it is necessary to consider the entire chain of the
processes as a single entity.

When these processes are analyzed, one has always to consider that the dynamic pressure of the solar wind and the inter-
planetary magnetic field (IMF) control the strength and the spatial structure of the magnetosphere-ionosphere current systems,
whose changes are at the origin of geomagnetic activity, i.e. of the variation of the Earth's magnetospheric-ionospheric field
as observed by space and ground-based measurements. Indeed, a significant amount of solar wind plasma can be dropped off
either directly in the polar ionosphere (polar cusp and cup) or stored in the equatorial central regions (the central plasma sheet,
the current sheet, etc.) of the Earth's magnetospheric tail, from where it is successively injected into the inner magnetospheric
regions such as, for instance, the radiation belts (*Gonzalez et al.*, 1994). The growth of the trapped particle population in the
inner magnetosphere produces a significant increase of the ring current, while the energy released from the magnetotail and
injected into the high latitude ionosphere, together with that directly deposited in the polar regions, is responsible for an en-
hancement of the auroral electrojet current systems (*McPherron*, 1995). The importance of studying these processes lies not
only in understanding the physical processes which characterise the solar-terrestrial environment, but also in its impact on the
technological and anthropic systems. Indeed, nowadays geomagnetic storms and substorms have become an important concern,
being potentially able to damage the anthropic infrastructures at ground and in space, as well as of harming human health (e.g.
Baker, 2001; *Ginet*, 2001; *Kappenman*, 2001; *Lanzerotti*, 2001; *Pulkkinen et al.*, 2017; *Hapgood*, 2019). As a consequence,
these processes play an important role in the space weather framework where the applications and societal relevance of the
phenomena are much more explicit than in solar-terrestrial physics (*Koskinen et al.*, 2017).

In this paper, we analysed a recent solar event occurred on August 20, 2018, which affected the Earth's environment on
August 25, 2018, giving rise to a G3 geomagnetic storm (i.e. when the Kp-index is equal to 7). We used a transversal approach
to describe the whole sequence of events from the Sun to the ground. We carried out an interdisciplinary study that, starting from
the analysis of the CME at the origin of the storm, of its propagation in the interplanetary space (hereafter, Interplanetary CME
- ICME), down to the analysis of the effects produced by the arrival of this perturbation in the magnetosphere, ionosphere and at
ground. We used measurements recorded on board satellites and at ground stations, in order to both follow the event evolution
and focus our attention on its ionospheric and geomagnetic effects measured at different latitudes/longitudes. Namely, we
discuss how the activity of the solar atmosphere and solar wind, travelling in the interplanetary space, has been able to deeply
influence the conditions of the Earth's magnetosphere and ionosphere or more generically has been able to deeply influence the
solar-terrestrial environment. We studied the propagation through the heliosphere of the CME, trying to take into consideration
the complicated and multifaceted nature of its interaction with the ambient solar wind and the magnetosphere, and on the
geomagnetic and ionospheric effects caused by this event. We exploit data from both satellites and ground-based observatories,
whose integration is fundamental to describe the effects on the Earth's environment produced by solar activity. We collected

and processed data from low-Earth orbit satellites, as for example ESA-Swarm and CSES (China Seismo Electromagnetic
Satellite), and from ground-based magnetometers. More than 80 magnetic observatories located all over the Globe (all those
available for the period under investigation), were involved in the analysis. To detect ionospheric irregularities, we used the
Rate Of change of electron Density Index (RODI) estimated from the electron density measured on board of CSES to study
the occurrence of electron density fluctuations. Finally, we evaluated possible Geomagnetically Induced Current (GIC) hazard
related to the main phase of the August 2018 geomagnetic storm, calculating the GIC index (*Marshall et al.*, 2010; *Tozzi et al.*,
2019) over two geomagnetic quasi-longitudinal array located in the European-African and in the North American sectors.

2   CME - Interplanetary propagation

The solar event that has been associated with the magnetospheric disturbances under analysis, occurred on August 20, 2018.
The source was an extremely slow CME that was not detected by SOHO LASCO (*Domingo et al.*, 2016; *Bothmer et al.*, 1995)
and would be therefore classified as a stealth CME (*Howard and Harrison*, 2013), if it was not imaged by STEREO-A COR2
(*Keiser et al.*, 2008; *Howard et al.*, 2013). While propagating, the ICME created an interplanetary shock that, at L1, advanced
the ICME itself by more than 30 hours. We note that the creation of a shock is not incompatible with a slow CME, since the
shock can be created by the expansion of the CME as it equalizes its pressure with the interplanetary plasma. In this section,
we present the characteristics of the CME at lift-off and of the ICME at L1, and put forward an interpretation of its propagation
by using a modified Drag Based Model (P-DBM, *Vrsnak et al.*, 2013; *Napoletano et al.*, 2018).

2.1   CME lift-off and interplanetary response

While the CME was hardly visible in the Field of View (FoV) of SOHO LASCO instruments, it could be easily seen in
STEREO-A COR2 images, with an angular width of $\simeq 45°$. The CME appears as a diffuse, slow plasma structure, entering
COR2 FoV on August 20, 2018 at 16:00 UT (± 1 hr) and reaching the FoV edge on August 21, 2018 at 08:00 UT (± 2 hr).
From this timing, we can estimate a PoS (Plane of Sky) velocity for the CME $V_{PoS} = (160 \pm 40)$ km/s.
 The most probable source for the CME is a filament eruption observed on August 20, 2018 at t_0= 08:00 UT at heliographic
coordinates $\theta_{Sun} = 16°, \phi_{Sun} = 14°$ on the solar surface (red circle in Figure 1). The filament ejection has been recorded by
SDO AIA (*Pesnell et al.*, 2019; *Lemen et al.*, 2011) imagers. Considering the relative positions of STEREO-A at the moment of
the CME lift-off, the source on the Sun, the information provided by the CDAW catalog of CME, and the hypothesis of radial
propagation, we can de-project the CME velocity and estimate its radial velocity at about 10 R$_{Sun}$ as $V_{rad} = (350 \pm 45)$ km/s.
In this respect, we report that the derived radial velocity is lower that the median of the CME speed distribution (*Yurchyshyn et
al.*, 2005), and confirms that CMEs associated with filament eruption tend to be slower than those associated with flares (e.g.,
Moon et al., 2002).
We also note that, at the time of lift-off, a sizeable coronal hole (yellow contour in Figure 1) was present at heliographic coor-
dinates $\theta_{Sun} \simeq -8°, \phi_{Sun} \simeq -20°$ that would generate a fast solar wind stream that could affect the CME propagation.
Figure 2 shows the ICME detection by Wind (*Lepping et al.*, 2019), DSCOVR (*Burt and Smith*, 2012), and ACE (*Stone et*
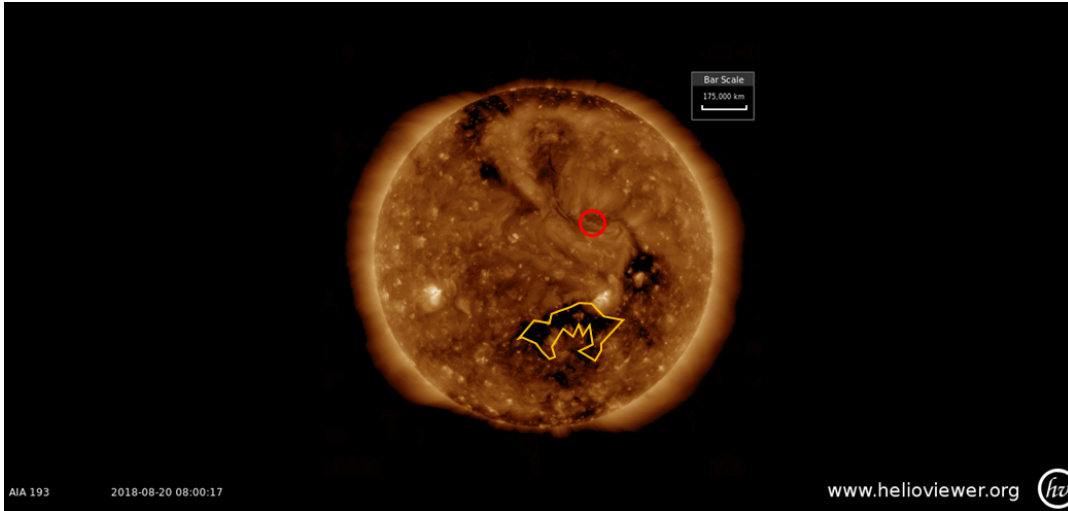
Figure 1. Image of the Sun with EUV SDO AIA193 at the time of the filament eruption. The red cirlce marks the position of the filament eruption associated with the CME; the yellow contour marks the position of the coronal hole. Image created using the ESA and NASA funded Helioviewer Project.

al., 2017) spacecrafts located at approximately L1 point. An interplanetary (IP) shock passed the three spacecrafts respectively at ∼05:37 UT, ∼05:42 UT, and ∼05:43 UT on August 24, 2018. This IP shock was characterized by small variation of the solar wind (SW) density ($\Delta n_{p,W} \approx 2.5$ cm^{-3}, $\Delta n_{p,D} \approx 2.8$ cm^{-3}, $\Delta n_{p,A} \approx 1.8$ cm^{-3}), velocity ($\Delta v_{SW,W} \approx 18$ km/s, $\Delta v_{SW,D} \approx 16$ km/s, $\Delta v_{SW,A} \approx 16$ km/s), dynamic pressure ($\Delta P_{SW,W} \approx 0.9$ nPa, $\Delta P_{SW,D} \approx 0.9$ nPa, $\Delta P_{SW,A} \approx 0.7$ nPa), and interplanetary magnetic field (IMF) strength ($\Delta B_{IMF,W} \approx 0.8$ nT, $\Delta B_{IMF,D} \approx 1.1$ nT, $\Delta B_{IMF,ACE} \approx 1$ nT). In agreement with the Rankine-Hugoniot conditions, the shock normal for the three spacecrafts was oriented at $\Theta_{SE,W} \approx -45°$ and $\Phi_{SE,W} \approx 130°$, $\Theta_{SE,D} \approx -45°$ and $\Phi_{SE,D} \approx 140°$, $\Theta_{SE,A} \approx -50°$ and $\Phi_{SE,A} \approx 100°$. The estimated shock speeds were respectively $v_{sh,W} \approx 300$ km/s, $v_{sh,D} \approx 300$ km/s, and $v_{sh,A} \approx 340$ km/s. Therefore, the predicted time of the impact of the IP shock onto the magnetosphere was at 06:14 UT (32 minutes after DSCOVR observations). The predicted location of the shock impact at the magnetopause, assuming a planar propagation, was at 7:00 ($\pm$00:15) LT (i.e. in the morning side of the magnetopause), corresponding, in the ecliptic plane, to $X_{GSE} = 5.0$ (± 0.2)R_E and $Y_{GSE} = -20.0$ (± 0.2)R_E (GSE is the Geocentric Solar Ecliptic reference system and R_E is the Earth's radius) (Figure 2g).

We note that, in principle, the creation of the shock is not incompatible with a slow CME since the shock can be created by the expansion of the CME as it equalizes its pressure with the interplanetary plasma. Nevertheless, this shock advanced the ICME by more than 30 hrs. Considering this long time separation, in our opinion this IP shock was not generated by the ICME under analysis.

The August 20 ICME included a significant magnetic cloud, observed at the Earth's orbit between August 25 at ∼12:15 UT and August 26 at ≈10:00 UT, whose boundaries are determined (*Burlaga et al.*, 1981) according to the the magnetic field behaviour conjoint with the temperature, the velocity and the density of protons, as depicted in Figure 2: the plasma temperature
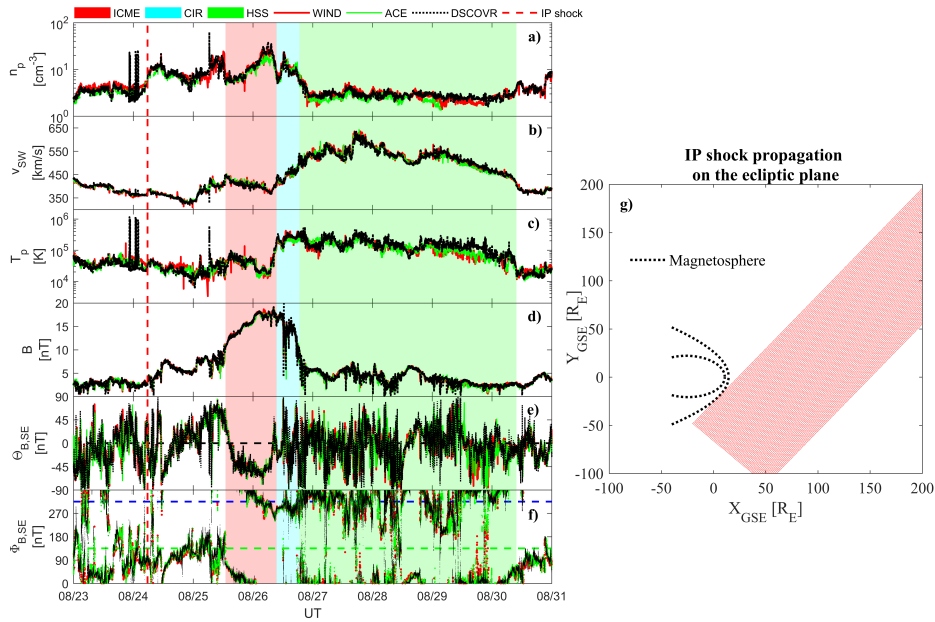
Figure 2. Solar wind parameters observed by WIND (red), ACE (green), and DSCOVR (black) spacecraft at L1: a) proton density; b) velocity; c) proton temperature; d) IMF intensity; e-f) IMF orientation (Θ_{SE} and Φ_{SE}, respectively) in the SE coordinate system. The vertical horizontal green and blue lines in panel f represent the expected orientation of the Parker spiral at L1. The red dashed line indicates the interplanetary shock as observed on August 24 at $\approx$ 5:43 UT (to match ACE measurements, both WIND and DSCOVR data were translated of 6 min and 1 min, respectively). The red shaded region identifies the ICME. The cyan and green shaded regions shows the CIR and the HSS, respectively; g) Interplanetary shock propagation in the ecliptic plane.

decreases from $\sim 9 \cdot 10^4$ K to $\sim 1.5 \cdot 10^4$ K; the total magnetic field increases to 16 nT, remaining there for approximately 12 hours; the magnetic field smoothly rotated, leading to pronounced and prolonged southward orientation (beginning at $\approx$14:30 UT on August 25) for approximately 22 hours; the solar wind speed fluctuated between $\sim$450 km/s and $\sim$370 km/s. A co-rotating interaction region (CIR) followed on August 26, the solar wind plasma showing a velocity (temperature) increase at $\approx$10:00 UT from $\sim$370 km/s ($\sim 4 \cdot 10^4$ K) to near $\sim$550 km/s ($\sim 30 \cdot 10^4$ K) at $\approx$12:20 UT, a density increase from $\sim 11 cm^{-3}$ to $\sim 30 cm^{-3}$, as the solar wind stream was transitioning into a negative polarity High Speed Stream (HSS).

2.2 A model for the propagation of the ICME

To describe the ICME propagation in the heliosphere we used the P-DBM (*Napoletano et al.*, 2018; *Del Moro et al.*, 2019) model. Considering the presence of the Coronal Hole (CH) on the Sun at the time of the CME lift-off and the CIR observations in in-situ data, we proposed the following scenario, where:

– the ICME propagation is longitudinally deflected by its interaction with the solar wind, as in equation 8 of *Isavnin et al.* (2013);
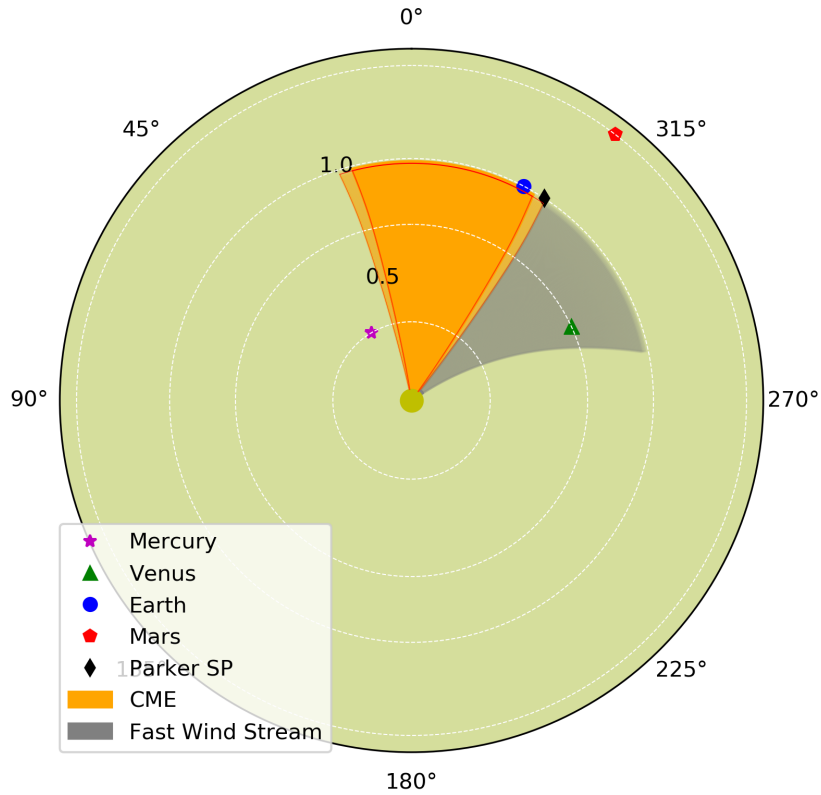
Figure 3. Scheme for the propagation of the CME in the inner heliosphere. The positions of the inner planets and Parker Solar Probe at the time of the ICME arrival at 1AU are represented by colored symbols. The ICME trajectory computed by the P-DBM is represented by the orange shadowed area. The lighter orange areas represent the 1σ uncertainty about the ICME trajectory from the 10000 different model runs. The grey shadowed area represents instead the fast solar wind stream.

- – the ICME is later overtaken by the fast solar wind stream from the identified CH at a distance r_{Mix};
- – r_{Mix} is computed considering the time for the CH to rotate in the appropriate direction plus the time for the stream to catch up with the ICME.

120 Applying the same philosophy behind the P-DBM, the longitude of the fast wind stream, generated by the CH, has been associated with a $2.5°$ error with a Gaussian distribution.

From 10000 runs of this model, the most probable result are: the ICME arrival time and velocity at 1AU are August 25, 2018 at t_{1AU}= 16:00 UT (±9 hr) and $V_{1AU} = 440$ (±70) km/s, respectively; the fast solar wind stream interacts with the ICME beyond $r_{Mix} = 1.1$ (±0.1) AU. These values agree nicely with the ICME actual arrival characteristics estimates as derived in

125   the previous section.

As discussed in *Richardson* (2018), a CIR would form by the interaction of a HSS with the preceding slower (in this case) ICME. Approximately one day later than t_{1AU}, the rotation of the Sun brings the CIR to sweep over Earth position, followed by a HSS. Last, this model predicts that the ICME that hit Earth, would instead miss Mars and possibly also the then newly launched Parker Solar Probe (PSP - *Fox et al.*, 2016). While no data is available for the PSP at that date, no solar particle event
130   was actually detected in the following days by the instrumentation on-board MAVEN (*Jakosky et al.*, 2015).

A graphical representation of this result is shown in Fig. 3, where the position of the inner planets and of the Parker Solar Probe at t_{1AU} are represented by colored symbols. The orange area represents the trajectory of the ICME, with lighter orange areas representing the 1σ uncertainty about its trajectory from the 10000 different model runs. The grey area represents the part of the inner heliosphere affected by the HSS at t_{1AU}.

135 ## 3   Magnetospheric-Ionospheric system response

A complete and accurate knowledge of the magnetospheric-ionospheric coupling and of its dynamics in response to the changes of the interplanetary medium conditions, is critical to many aspects of the space weather. It is, indeed, well-known that the changes of the IMF and of the solar wind features, in terms of magnetic field orientation, plasma density, velocity, etc., is capable of generating a fast increasing of the magnetospheric-ionospheric current intensities which manifests in multiscale
140   and rapid fluctuations of ground-based magnetic field. The response of the magnetosphere-ionosphere system to interplanetary changes is however the consequence of both directly-driven, i.e., large scale plasma convection enhancement, and triggered-internal phenomena, such as loading-unloading mechanisms, sporadic plasma energizations in the magnetotail, bursty-bulk flows (*Milan*, 2017). The response of such a system is strongly dependent on the magnetospheric plasma internal state, with a specific emphasis to the magnetotail central plasma sheet status. The result of the interplay between internal dynamics
145   and directly-driven processes is a very complex dynamics showing scale invariant features typical of non-equilibrium critical phenomena (*Consolini et al.*, 1996; *Consolini*, 1997; *Consolini and De Michelis.*, 1998; *Consolini*, 2002; *Lui et al.*, 2000; *Sitnov et al.*, 2001; *Uritsky and Pudovkin*, 1998; *Uritsky et al.*, 2002). In a series of recent papers (*Alberti et al.*, 2017, 2018; *Consolini et al.*, 2018) it has been clearly shown the existence of a separation of timescales between directly-driven and triggered internal timescales in the response of the Earth's magnetosphere-ionosphere current systems as estimated by means of geomagnetic
150   indices in the course of magnetic storms and substorms. This separation of timescales is one of the fingerprints of the complex character of the geomagnetic response, which makes very difficult to get a reliable forecast of its short timescale dynamics.

In this section, we investigate the magnetospheric-ionospheric response during the August 2018 geomagnetic storm. On one hand, the magnetosphere accumulates energy from the solar wind and dissipates it through geomagnetic storms, driving large electrical currents. On the other hand, these currents close down into the ionosphere, producing large scale magnetic
155   disturbances, such as the auroral electrojects, the DP-2 current system, prompt penetrating electric field and so on (*Piersanti et al.*, 2017; *Pezzopane et al.*, 2019, and references therein). Some of these features and phenomena will be discussed in the next sections for the investigated August 2018 geomagnetic storm.

3.1 Magnetosphere

Figure 4 a) shows the response of the magnetosphere to the the front boundary of the magnetic cloud. According to the *Shue et al.* (1998) model, the magnetopause nose moves inward up to $\sim$7.1 R_E. Indeed, the shape of the magnetospheric field lines before (black lines) and soon after (red lines) the arrival of the magnetic cloud, evaluated by means of the TS04 model (*Tsyganenko and Sitnov*, 2005) shows a large field erosion. Correspondingly, GOES 14 (panels b, d and f) and GOES 15 (panels c, e and g) show, on August 25 at $\sim 06:30$ UT, a strong compression ($\Delta B_{z,G14} = 10$ nT and $\Delta B_{z,G15} = 22$ nT) of the magnetic field coupled with a stretching of the magnetotail field lines, due to the southward switching of the IMF orientation (*Villante and Piersanti*, 2011; *Piersanti and Villante*, 2016; *Piersanti et al.*, 2017, as already found by). This situation completely changes between August 25 at $13:55$ UT and August 26 at $10:25$ UT, corresponding to the lowest values of the southward IMF ($B_{z,IMF}$) in the magnetic cloud. In fact, both GOES 14 and GOES 15 show a strong decrease of B_z (panels f and g), interpreted in terms of magnetic reconnection between the magnetospheric field and the strong $B_{z,IMF}$ (~ -20 nT) observed in the corresponding interval (*Piersanti et al.*, 2017, and references therein). Interestingly, both GOES satellites show a huge increase of the B_x component (panels b and c) and a negative, then positive variation in the B_y component (panels d and e). This behaviour is the signature of a strong stretching and twisting of the magnetospheric field lines during the main phase of the geomagnetic storm (*Piersanti et al.*, 2012, 2017). This scenario is confirmed by a modified *Tsyganenko and Sitnov* (TS04* 2005) model indicated by red dashed lines in Figure 4. Model changes include: the magnetopause and the ring current alone, during the main phase; the concurring contribution of both the ring and the tail currents, during the recovery phase. TS04* model represents very well the magnetospheric observations at geosynchronous orbit, with an average correlation coefficient (r) for the three magnetic field components: $r =$0.92 for GOES14; $r =$0.75 for GOES15.

Figure 5 (box A) shows the CSES (China Seismo Electromagnetic Satellite) satellite (*Shen et al.*, 2017) magnetic observations (*Zhou et al.*, 2019) along North-South (B_N - left panel), East-West (B_E - central panel) and Vertical (B_C - right panel) components after removing the internal and crustal contributions to the Earth's magnetic field (using the CHAOS-6 model *Finlay et al.*, 2016).

CSES is a Chinese satellite launched on February 11, 2018 hosting, among others, a fluxgate magnetometer, an absolute scalar magnetometer, two Langmuir probes, and two particle detectors. The satellite orbits at about 500 km of altitude (Low Earth Orbit - LEO) in a quasi-polar Sun-synchronous orbit and passes at about 14 and 2 local time (LT) in its ascending and descending orbits, respectively.

As expected (*Villante and Piersanti*, 2011), the greatest variations are observed along the horizontal components, where both the magnetospheric and ionospheric currents play a key role.

In order to quantify both the magnetospheric and ionospheric origin contributions at CSES orbit, we applied the MA.I.GIC. model (*Piersanti and Carter*, 2019) to discriminate between different time scales contributions in a time series. The results obtained are shown in Figure 5 (box B). Upper and lower panels report high ($\sim$25 μHz $<$ f $<\sim$ 3 mHz; f being the frequency) and low frequency (~ 2.3 μHz $<$ f $<\sim$ 25 μHz) components observations, respectively. The low frequency behaviour shows a strong and rapid decrease along the North-South direction during the main phase of the geomagnetic storm and a long lasting
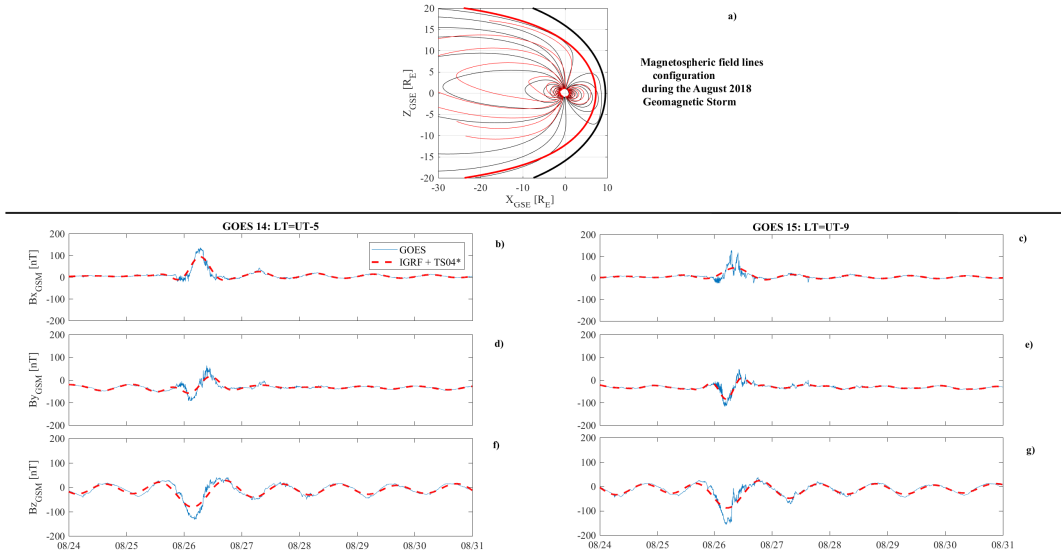
Figure 4. panel a): Magnetospheric field lines configurations as predicted by TS04 model before (black lines) and after (red lines) the passage of the front boundary of the magnetic cloud; panels b), d) and f): magnetospheric field observations along X_{GSM} (b), Y_{GSM} (d) and Z_{GSM} (f) at GOES 14 (LT=UT-5) geosynchronous orbit; panels c), e) and f): magnetospheric field observations along X_{GSM} (b), Y_{GSM} (d) and Z_{GSM} (f) at GOES 15 (LT=UT-5) geosynchronous orbit; red dashed lines represent the IGRF+TS04* model prevision.

increase during the recovery phase. On the other hand, $B_{E,LF}$ shows a negative then positive variation during the main and the recovery phase, respectively. $B_{C,LF}$ is characterized by negligible variations. This behaviour is consistent with magnetospheric origin field variations induced by the action of both the symmetric part of the ring current and tail current along $B_{N,LF}$ and

195 of the asymmetric part of the ring current along $B_{E,LF}$ (*Piersanti et al.*, 2017). It is confirmed by the comparison between the CSES magnetospheric origin contribution and the TS04* model (red lines in Figure 5, box B), in which we considered both the magnetopause and ring current alone during the main phase, and both the ring current and tail current alone during the recovery phase. It can be easily seen TS04* well represents the along $B_{N,LF}$ variations, while it is not able to reproduce the $B_{E,LF}$ variations. This would suggest that the partial ring current field (with the effect of the field-aligned currents associated with the

200 local time asymmetry of the azimuthal near-equatorial current), which is not included in the TS04 model, plays a relevant role.

The high frequency components show large variations along both $B_{N,HF}$ and $B_{E,HF}$. This behaviour is consistent with the contributions due to the variations of the ionospheric current systems and to the magnetospheric-ionospheric coupling processes. In fact, the huge positive then negative variations observed during the main phase along both the horizontal components can be imputable to the loading-unloading process between the magnetosphere and the ionosphere (*Consolini and De Michelis*,

205 2005; *Piersanti et al.*, 2017). On the other hand, the variations observed during the recovery phase, which are positive on average, can be due to the ionospheric DP-2 current system (*Villante and Piersanti*, 2011; *Piersanti and Villante*, 2016; *Piersanti et al.*, 2017).
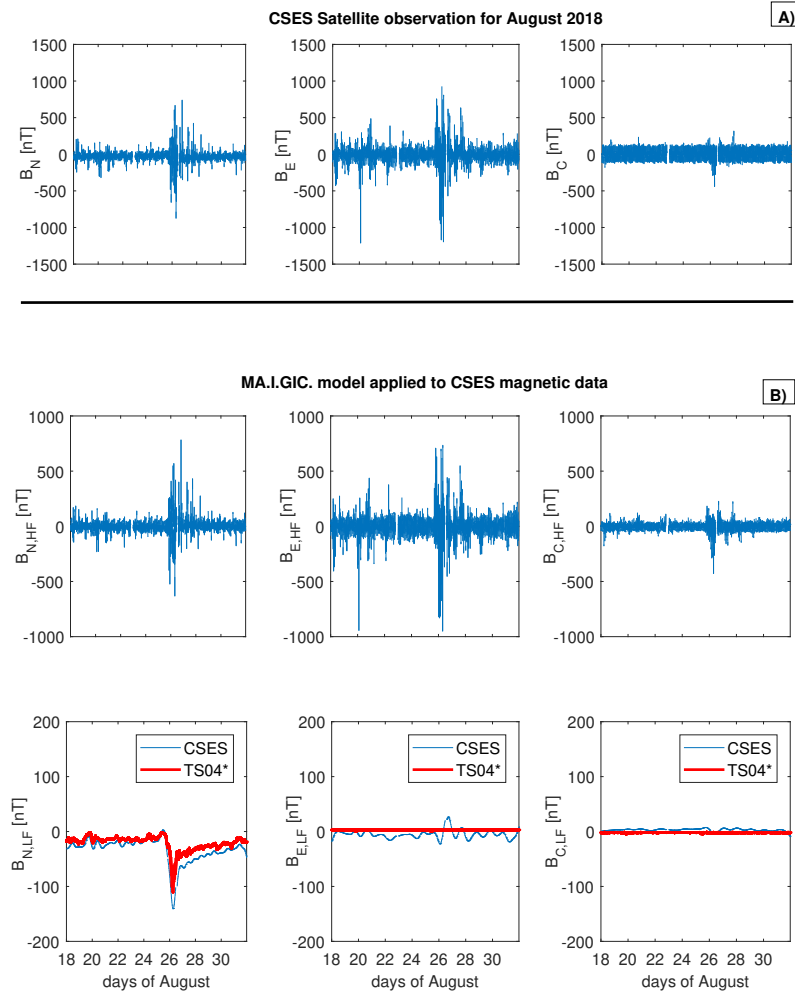
Figure 5. Box A) Magnetic field observations at CSES orbit along geographic North-South (left panel), East-West (middle panel) and vertical (right panel); Box B) MA.I.GIC. model applied to CSES magnetic data: upper panels show the high frequency time scales ($\sim$25 μHz $<$ f $<\sim$ 3 mHz; f being the frequency) for the three components of the observed field; lower panels show the low frequency time scales ($\sim$ 2.3 μHz $<$ f $<\sim$ 25 μHz) for the three components of the observed field. Red lines represent the TS04* model previsions along CSES orbit.

3.2 Ionospheric response

The ionospheric plasma is often characterized by irregularities and fluctuations in the plasma density, especially during active solar conditions. In order to characterize such irregularities, we evaluated the RODI, a parameter derived from the electron density (see Appendix A) recorded by the CSES satellite (*Wang et al.*, 2019).

Figure 6 shows RODI values for August 25, 26, and 27, 2018, in which nighttime semi-orbits (around 02:00 LT) are shown separately from daytime semi-orbits (around 14:00 LT).
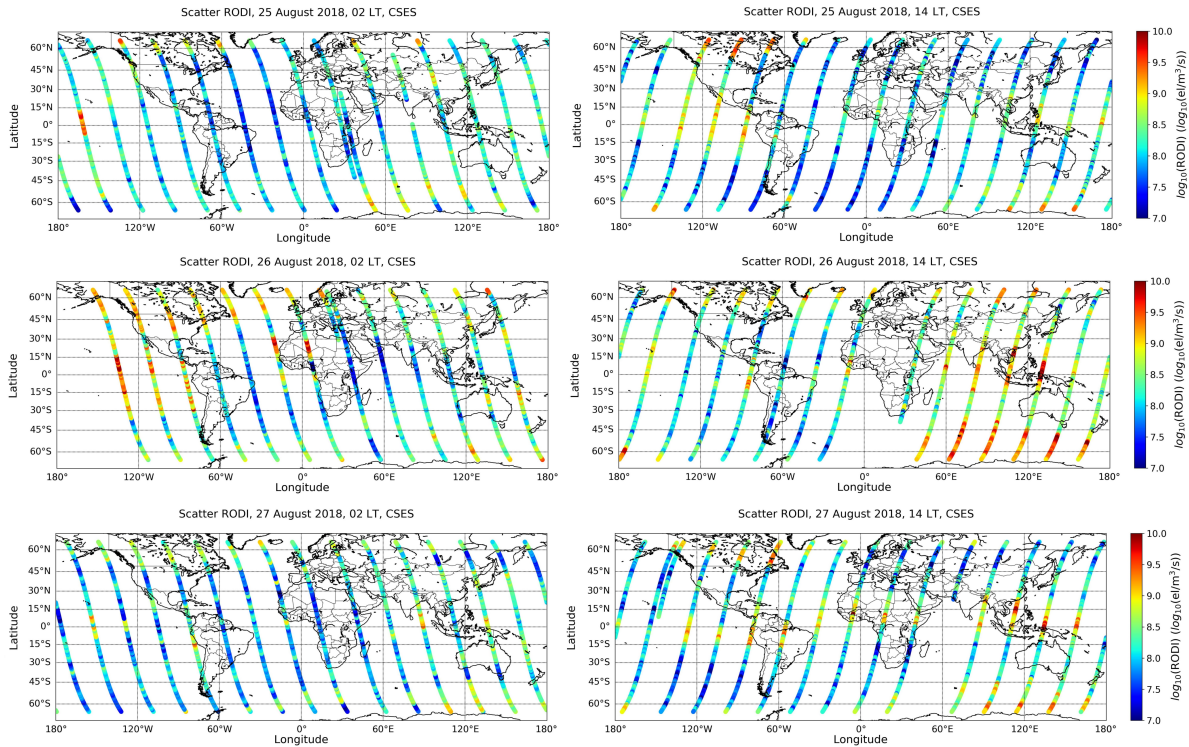
Figure 6. RODI calculated for August 25, 26, and 27, 2018. Scale is logarithmic. Coordinates are geographical. Left panels show nighttime semiorbits (ascending), while right panels show daytime semiorbits (descending). Time increases leftward. Electron density values are recorded by CSES.

A significant high RODI values, spreading all over the meridian during the main phase of the storm (August 25 and 26, 2018, especially the latter), for both nighttime and daytime, is clearly seen, while on August 27, 2018, the RODI comes back to lower values. This behaviour can be explained in terms of the presence, during the main phase, of ionospheric irregularities, especially at auroral and low latitudes. To understand whether this significant increase of irregularities could have caused space weather effects on navigational systems, we have considered vertical total electron content (vTEC) data measured by Swarm satellites (*Friis-Christensen et al.*, 2006, 2008) to look for some loss of lock on GPS (Global Positioning System *Jin and Oksavik*, 2018, and references therein). Only vTEC data with corresponding elevation angles $\geq 50°$ have been taken into account. We have

considered vTEC data recorded by each of the three satellites (A, B, and C) of the Swarm constellation and corresponding to each PRN (Pseudo Random Noise) satellite in view. No loss of lock has been found, contrary to what happened, for instance, during the well-known and much more intense (i.e. Dst=−230 nT) St. Patrick storm occurred on March 17, 2015 (*Jin and Oksavik*, 2018; *De Michelis et al.*, 2016; *Pignalberi et al.*, 2016), where vTEC measurements highlighted many loss of lock (figures not shown). The fact that no loss of lock has been found during the August geomagnetic storm means that the event was weak in terms of space weather effects on navigational systems.

This fact is also supported by Figure 7, where rate of change of TEC index (ROTI) values (ROTI is calculated as RODI but considering TEC values in place of electron density values, for a defined GPS satellite in view) from Swarm A are shown for PRN 8 on August 26, 2018, and for PRN 15 on March 17, 2015. It is clear, from this figure, that a loss of lock occurs when ROTI saturates, a feature that rarely happens on August 26, 2018 and more in general during the entire period under analysis.

4 Magnetic effects at ground

Space weather predictions and geomagnetic storms intensities are normally measured on the basis of well known geomagnetic indices. Anyway, as these indices are evaluated using ground observations (typically via magnetometers), it is crucial to improve the knowledge of the effect of each magnetospheric and ionospheric current at ground. In this section, we focused on the ground magnetic response in terms of magnetospheric and ionospheric currents, and on the effects that those currents generated on the Earth's surface. GICs are one of the main ground effects of space weather events driven by solar activity (*Pulkkinen*, 2015; *Pulkkinen et al.*, 2017; *Carter et al.*, 2016; *Piersanti and Carter*, 2019). Since GICs represent the end of the space weather chain extending from the Sun to the Earth's surface, to complete the description of August, 25 2018 geomagnetic storm, an estimation of the amplitude of geomagnetically induced currents and of the associated risk level, to which power grids have been exposed during this storm, is also presented.

4.1 Geomagnetic field response

To analyse the magnetic effects at ground during the geomagnetic storm, we selected 83 magnetic observatories from INTERMAGNET magnetometer array network. INTERMAGNET is a consortium of observatories and operating institutes that guarantees a common standard of data released to the scientific community, thus making it possible to compare the measurements carried out at different observation points. The distribution of the selected observatories is reported in Figure 8 and covers the geographic latitudes between −80° and 80° providing a continuous sampling of the geomagnetic field. Although INTERMAGNET provides geomagnetic data with a time resolution down to 1 second, for our purpose a time resolution of 1 minute was sufficient. We have considered the horizontal magnetic field component (H) and focused our analysis on a period of seven days (from August 23 to August 29), during which the storm occurred. The selected period allows us to follow the evolution of the magnetic disturbance recorded at ground, during the geomagnetic storm. Moreover, we use the model of (*Thomas and Shepherd*, 2018) based on the Super Dual Auroral Radar Network (SuperDARN) to analyses the ionospheric convection during the same period. SuperDARN is an international network of more than 35 high-frequency (HF) radars which
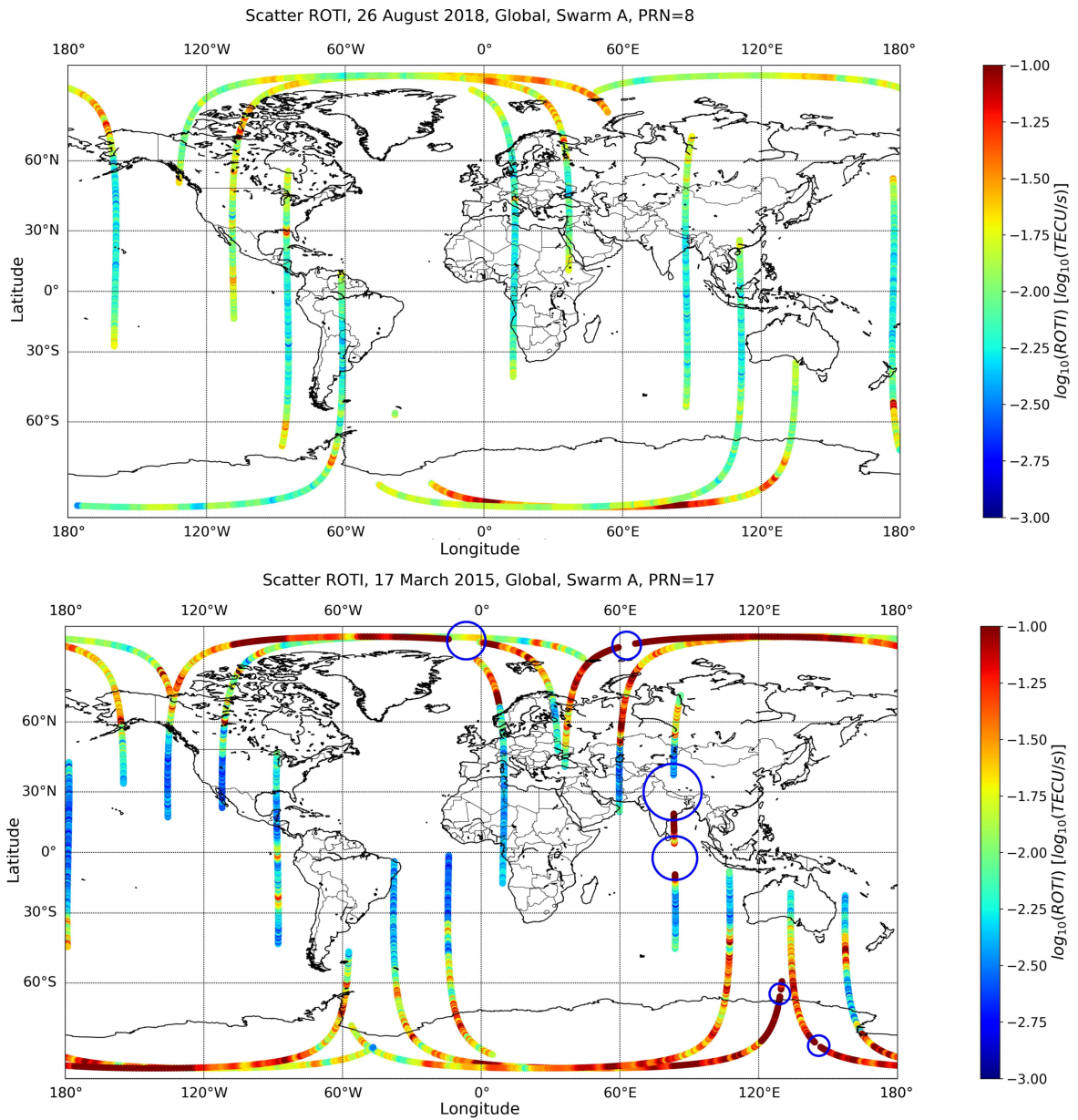
Figure 7. ROTI values from Swarm A calculated (top panel) for PRN 8 on August 26, 2018 and (bottom panel) for PRN 17 on March 17, 2015. Loss of lock visible in the figure, highlighted by blue circles, correspond to parts of the trace where ROTI saturates.

has been implemented for the study of the ionosphere and upper atmosphere at sub-auroral, auroral and polar cap latitudes in both Northern and Southern Hemispheres (*Chisham et al.*, 2007; *Nishitani et al.*, 2019).
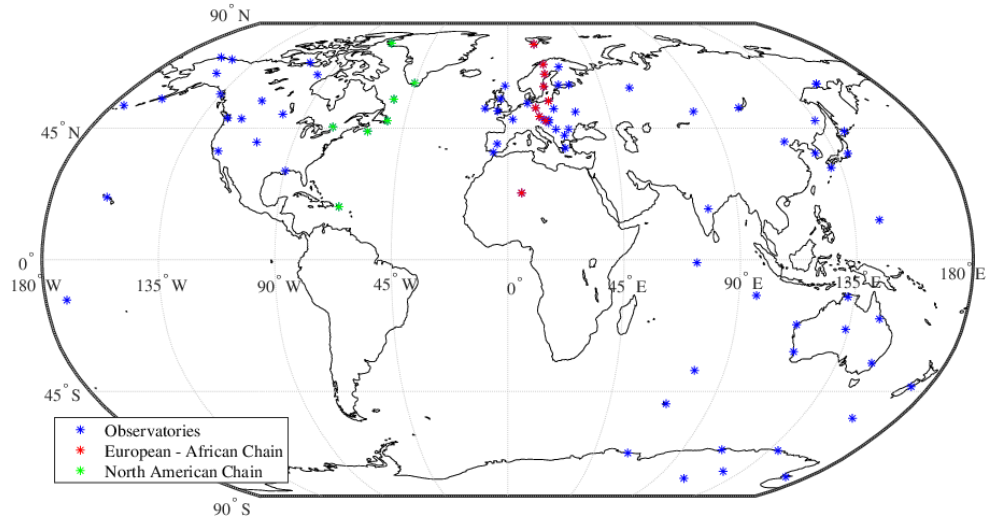
Figure 8. Geographical positions of the selected 83 INTERMAGNET geomagnetic observatories (blue stars). Red and green stars identifies a European-African and North American almost longitudinal chains, respectively, selected for the GIC analysis. The map is in geographic coordinates.

Figure 9 shows the daily distributions of the intensity of the horizontal magnetic field component obtained considering data recorded simultaneously by the selected magnetic observatories during the analysed period. The figure reports: on the left the values of the SYM-H index (*Iyemori*, 1990; *Menvielle*, 2011), which can be used to monitor the geomagnetic activity and more in detail the ring current intensity during the geomagnetic storm; in the middle, daily polar view maps of the horizontal field magnitude in the Northern Hemisphere and of the ionospheric convection patterns derived from the model of (*Thomas and Shepherd*, 2018) based on SuperDARN observations; on the right, the cylindrical projection view of the same magnetic field component. Data are reported in geomagnetic latitude and magnetic local time (MLT, *Baker*, 1989).

Of particular interest is the analysis of the effects of the ionospheric and magnetospheric currents on the geomagnetic field. For this reason, we have removed the main field from the data and considered only the magnetic fields generated by the electric currents in the ionosphere and magnetosphere (i.e. the so-called magnetic field of external origin). For this purpose, for each ground station, we removed the internal and the crustal origin fields as modeled by CHAOS-6 (*Finlay et al.*, 2016).

Thus, the horizontal field magnitude values reported in Figure 9 describe the magnetic field perturbations at ground due to external sources. The main contributions to this external field, producing relevant signatures in magnetic field observations, are the polar ionospheric currents, such as the auroral electrojets, and the magnetospheric currents such as the Chapman-Ferraro currents and (in particular) the magnetospheric ring current (*Rishbeth and Garriot*, 1993; *Hargreaves*, 1992). These current systems are almost always present even during geomagnetic quiet periods but show a significant variability during the disturbed periods (*De Michelis et al.*, 1997). The maps reported in Figure 9 show the effect due to the eastward and westward auroral electrojets. These two polar current systems, which are the most prominent currents at auroral latitudes, produce at ground a magnetic field perturbation that is characterized by a positive excursion of the horizontal field magnitude in the case of the eastward electrojet, flowing in the afternoon sector, and a negative one in the case of the westward electrojet flowing through the morning and midnight sector (*De Michelis et al.*, 1999). It can be especially seen from the data reported in the polar view maps (central column in Figure 9). We noticed that these currents are always present but their intensities increase during the main phase of the geomagnetic storm (*Ganushkina et al.*, 2018). Even their spatial distribution changes. Indeed, the magnetic disturbance, associated with these electric currents, tends to shift towards lower latitudinal values drastically during the geomagnetic storm. On August 26 the westward electrojet is extremely intense and around midnight the effect at ground due to the substorm electrojet current is recognizable, too. The associated disturbance fields cover the geomagnetic latitudes from $50°$ to $75°$ on the nightside. Looking at the ionospheric convection as derived from the statistical model of (*Thomas and Shepherd*, 2018) and considering that mean daily values of the IMF and solar wind velocity have been used as input to the model, the convection patterns match the expansion to lower latitudes observed in the magnetic disturbance evolution during the extreme driving conditions ($E_{SW} \geq 4.0 mV/m$) that characterise the period under study after the southward rotation of the IMF. In fact, also the convection maps computed from the SuperDARN measurements at 2 minutes resolution (not shown) display that the auroral convection zone expands equatorward to $50°$ geomagnetic latitude during the geomagnetic storm. The expansion of the convection pattern is related to the dayside reconnection forming new open field lines once the IMF turned southward in late August 25.

The panels on the right column of Figure 9 show the effect due to the ring current that is responsible for a decrease of the magnetic field intensity at low and mid latitudes, during the development of the geomagnetic storm. As known, the intensity of the ring current increases during the main phase of a geomagnetic storm, because of the injection of energetic particles from the magnetotail in the equatorial plane, and gradually decays during the recovery phase. The time evolution of the ring current, through the time evolution of its associated disturbance field, is clearly visible in our data. During the main phase of the storm (August 26), the increasing of the ring current flowing in the westward direction produces a strong depression of the horizontal field magnitude, as can be seen by the blue region at mid/low-latitudes of the map corresponding to August 26, on the right-side of Figure 9. In the days following the main phase the magnetic field perturbation associated with the ring current is still visible at low and mid latitudes, although its amplitude rapidly decreases. We can conclude that the magnetic field perturbations on the ground due to the arrival of the solar perturbation are clearly recognizable in the recorded data and are well in agreement with what is expected from a theoretical point of view (*Piersanti et al.*, 2017, and references therein).

4.2 Ground magnetic effects

Fluctuations of the geomagnetic field happening during geomagnetic storms or substorms are responsible for an induced geoelectric field at the Earth's surface that, in turn, originates GIC that may represent an hazard for the secure and safe operation of electrical power grids and oil/gas pipelines. For instance, for the case of power transmissions, GICs represent a hazard due to their frequency. Indeed, the power spectrum of the originating geoelectric field is dominated by frequencies smaller than 1 Hz and this makes the GIC a quasi-DC current compared to the 50-60 Hz AC power systems, with the consequence to temporarily or permanently damage power transformers (*Pulkkinen et al.*, 2017, and references therein).

As a proxy of the geoelectric field, and hence of GIC intensity, the GIC index (*Marshall et al.*, 2010) is calculated using the approach proposed by (*Tozzi et al.*, 2019). Among the proxies of the geoelectric field resorting to magnetic data only, this index has two main advantages: 1) it represents the geoelectric field better than other commonly used quantities (i.e. dB/dt or other geomagnetic activity indices), 2) its values are used to determine the risk level to which power networks are exposed during space weather events (*Marshall et al.*, 2011). Since the components of the geomagnetic field relevant for the induction of the geoelectric field are the horizontal ones, i.e. the Northward (X) and Eastward (Y) components, the GIC index is calculated for both of them. Particularly, GIC_y and GIC_x indices, are obtained using 1-minute of X and Y components, respectively, as observed at the geomagnetic observatories aligned along two latitudinal chains crossing North America and Europe-Africa. These two sets of observatories satisfy the condition to be characterised by geomagnetic longitudes that are spread over a range of $\approx 40°$ around a central longitude. In the case of the North American chain the central geomagnetic longitude is about 17° E and the observatories used for this chain, indicated by their IAGA codes and ordered from high to low geomagnetic latitude, are: THL, NAQ, STJ, OTT, SBL, SJG, KOU. The central geomagnetic longitude of the European-African chain is about 105° E and the corresponding observatories, listed as above, are: HRN, ABK, LYC, UPS, HLP, NGK, BDV, TAM. Details on the observatories of the two chains can be found in Table 1.

To have an idea of the maximum GIC intensity produced by the August 26, 2018 geomagnetic storm, we calculated GIC_x and GIC_y indices for the geomagnetic observatories of the two chains and then picked out the maximum values reached by both GIC indices from August 25, 2018 at 18:00 UT to August 26, 2018 at 18:00 UT (i.e. the most geomagnetically disturbed conditions) and plotted them as a function of geomagnetic latitude in Figure 10. The two curves displayed in both panels a) and b) of Figure 10 refer to the North American (red) and to the European-African (blue) observatories chains, respectively. As expected, the latitudinal dependence of the maximum GIC intensity shows an increase with increasing latitude with a steepening of the curve around 60° N and then a substantial decrease at the highest latitude, near the geomagnetic pole. This reflects the geometry and the features of the current systems responsible for time variations of the geomagnetic field originating the induced geoelectric field. High-latitudes are affected by the effects of the auroral electrojets whose intensity undergo dramatic variations even increasing up to 4–5 times its quiet time value (*Smith et al.*, 2017). Low and mid latitudes are mainly affected by the ring current that produces variations of the geomagnetic field that are less effective for GICs building up. So, the peaks around 65-75° N, well visible in Figure 10, can be interpreted in terms of the position of the auroral oval and hence of the auroral electrojets flowing. Moreover, as can be observed by Figure 10 both the European-African and North

Table 1. Details of the geomagnetic observatories used in the study, from left to right columns indicate: the name and IAGA code of the observatory, geomagnetic latitude, geomagnetic longitude, MLT* representing the number of hours to add to UT 00:00 to obtain MLT location of each observatory.

North American chain				European-African chain			
Observatory	Geomag. Lat.	Geomag. Long.	MLT*	Observatory	Geomag. Lat.	Geomag. Long.	MLT*
	$°N$	$°E$	hour		$°N$	$°E$	hour
Thule (THL)	87.11	14.74	0.98	Hornsund (HRN)	74.08	124.94	8.33
Narsarsuaq (NAQ)	69.36	38.68	2.58	Abisko (ABK)	66.19	114.26	7.62
St John's (STJ)	56.59	24.69	1.65	Lycksele (LYC)	62.71	110.71	7.38
Ottawa (OTT)	55.1	-3.6	-0.24	Uppsala (UPS)	58.51	106.24	7.08
Sable Island (SBL)	53.33	15.28	1.02	Hel (HLP)	53.23	104.67	6.98
San Juan (SJG)	27.76	6.95	0.46	Niemegk (NGK)	51.81	97.75	6.52
Kourou (KOU)	14.33	20.47	1.36	Budkov (BDV)	48.72	97.79	6.52
				Tamanrasset (TAM)	24.44	82.34	5.49

American chains provide peaks of the GIC indices at different geomagnetic latitudes. In detail, the peak along the European-African chain seem to occur at latitudes smaller than that along the North American chain. Such observation can be explained in terms of the MLT at which the maxima of the GIC indices occur at the observatories of the two chains: around (01:00 ± 01:00) MLT for the European-African chain and around (21:00 ± 01:00) MLT for the North American chain. Indeed, as can be deduced by Figure 9, especially by looking at the worldwide view of the horizontal field magnitude, the maximum variation of the horizontal component of the geomagnetic field recorded on August 26 around 01:00 MLT occurs at latitudes lower than that observed at 21:00 MLT. The most the auroral oval expands towards lower latitudes, the smallest the latitude where the steepening of the maximum GIC index occurs. Since, as already mentioned, the advantage to use the GIC index relates to the availability of an associated risk level scale, Figure 10 also displays colored dashed lines that indicate the boundaries between adjacent risk levels. This risk level scale has been introduced and defined by *Marshall et al.* (2011), it consists of four risk levels going from "very low" to "extreme", each associated with defined ranges of the GIC_x and GIC_y indices. This scale is based on a large occurrences of faults or failures of worldwide power grids and represents a probabilistic description of the threat, the risk level providing the probability to have a fault; detailed information on this scale are given in *Marshall et al.* (2011). Results shown in Figure 10 tell that, for the analysed geomagnetic storm and for the same latitudes, power networks located along the European-African chain have been exposed to higher risk levels than those located along the North American chain.

As in the case of the ionospheric response, we repeated the analysis (same method and observatories), using data recorded during the 2015 St. Patrick geomagnetic storm (Figure 11), to have a quantitative comparison of the effects of the two storms. There are evident similarities between Figure 11 and Figure 10, but some interesting differences can be highlighted. First, although 2015 St. Patrick storm was slightly more intense than August 26, 2018 geomagnetic storm (minimum values of

Sym-H index of -234 and - 206 nT, respectively), its maximum value of the GIC index is lower and occurs mainly on the dayside for both chains of observatories. This difference could be ascribed to the different location of the shock impact at the magnetopause: in the morning for the 2018 August storm and on the nose of the magnetopause for the 2015 St. Patrick storm. Second, during St. Patrick's storm the southern boundary of the auroral oval has experienced a larger equatorward expansion. This can be deduced by the value of the southernmost latitudes exposed to risk levels higher than "moderate". In the case of the August storm, these are larger than around $60°$ N, while during the St. Patrick storm they decreased to around $45\text{-}50°$ N. Last, the maximum values of GIC index at low-mid latitudes are very low for both geomagnetic storms but slightly higher in the case of St. Patrick storm. This suggests a greater participation of other current systems as, for instance, the ring current.

5   Summary and discussion

The solar event that has been associated with the August 25, 2018 geomagnetic storm occurred on August 20, 2018. The most probable source for the CME is a filament eruption observed at 08:00 at heliographic coordinates $\theta_{Sun} = 16°, \phi_{Sun} = 14°$ on the solar surface (Pink post in Figure 1). The filament ejection has been recorded by SDO EUV imagers.

In order to reconstruct the ICME behavior in interplanetary space and to link the results from remote-sensing and in-situ data, we propagate the CME in the heliosphere in the framework of the P-DBM (*Napoletano et al.*, 2018) model under the hypotheses that: the ICME propagation is longitudinally deflected by its interaction with the solar wind; the ICME is later overtaken by fast solar wind stream from the identified coronal hole at a distance r_{mix}, evaluated considering the concurring contribution of both the time for the CH to rotate in the appropriate direction and the time for the stream to catch up with the ICME. It results that the ICME arrival time and velocity at 1AU are: August 25, 2018 at 16:00 UT (± 9 hr) and (440 ± 70) km/s. This scenario is confirmed by the solar wind observations at L1. In fact, ACE, WIND and DSCOVR satellites detected the ICME arrival on August 25, 2018 at $\sim$12:15 UT.

As a consequence of the magnetic cloud arrival, the magnetospheric field lines configuration reveal a large magnetopause erosion from 10 R_E to 7.1 R_E as both predicted by the TS04 model and observed by GOES14/GOES15 satellites, caused by the gradual depletion of $B_{z,IMF}$. In addition, the magnetosphere is stretched and twisted as a consequence of the action of the magnetopause and the ring current alone between August 25, 2018 at 13:55 UT and August 26, 2018 at 8:15 UT (corresponding to the main phase of the geomagnetic storm, at ground), and of the concurring contribution of both the ring and the tail currents between August 26, 2018 at 8:15 UT and August 31, 2018 (corresponding to the recovery phase of the geomagnetic storm, at ground). This scenario is confirmed by the simulation of a modified TS04 model set with the previous magnetospheric current assumptions, which well represents the behaviour of the observations at geosynchronous orbit (red dashed lines in Figure 4). A similar situation is obtained at LEO orbit on CSES satellite (figure 5), where the magnetospheric origin field variations (low frequency contributions) are induced by the action of both the symmetric part of the ring current and tail current along $B_{N,LF}$ and of the asymmetric part of the ring current along $B_{E,LF}$ (*Piersanti et al.*, 2017), as confirmed by the TS04* model previsions. Differently from GOES observations, CSES shows also variations at higher frequencies ($\sim$0.025 mHz < f <$\sim$ 3 mHz), which are of both ionospheric current systems and the magnetospheric-ionospheric coupling origin

contributions. Our interpretation of the huge positive then negative variations observed during the main phase along both the horizontal components, is due to the loading-unloading process between the magnetosphere and the ionosphere (*Consolini and De Michelis*, 2005; *Piersanti et al.*, 2017). On the other hand, the variations observed during the recovery phase are due to the ionospheric DP-2 current system (*Villante and Piersanti*, 2011; *Piersanti and Villante*, 2016; *Piersanti et al.*, 2017).

At ground, during the main phase, the disturbance fields observed at latitudes between $50°$ and $75°$, on the night side, are due to the intensification of the westward auroral electrojet. In addition, on August 26, 2018, the pattern of the auroral electrojects are consistent with a ICME impacting on the morning side of the magnetosphere. In fact, as expected (*Wang et al.*, 2010; *Piersanti and Villante*, 2016; *Pilipenko et al.*, 2018), the greater disturbance for both the westward and eastward electrojects are located around 7:00 LT, (central panels of Figure 9). In addition, it is interesting to note that the large values of the westward electroject could be due to the concurring contributions of the magnetic cloud and CIR that increase the unloading process from the tail to polar region (*Consolini and De Michelis*, 2005, and references therein). In the same day, the injection of energetic particles from the magnetotail in the equatorial plane increased the ring current, generating at lower latitudes strong depression of the horizontal field magnitude on the Earth's surface (right panels in Figure 9). During the recovery phase, we observed a return of the horizontal component of the geomagnetic field to pre-storm values due to the decrease the ring current amplitude(*Piersanti et al.*, 2017).

From an ionospheric point of view, to figure out whether the significant increase of electron density irregularities recorded in terms of RODI, especially during the main phase, affected navigation systems, we estimated loss of lock from the vTEC Swarm data. No loss of lock has been found, which means that the event was weak in terms of space weather effects on navigation systems. This fact is supported by Figure 7 showing that loss of lock occurs mainly for really high values of ROTI, values never recorded during the period under analysis.

The amplitude of the geomagnetically induced currents index (*Marshall et al.*, 2011; *Tozzi et al.*, 2019), evaluated during the August 2018 geomagnetic storm, reached very high values above $60°$ N of geomagnetic latitude. A direct comparison to St. Patrick event showed that although the different storm intensities, the GIC hazard was extreme during the August 2018 event, while "only" high in the March 2015 event. On the other hand, both storms present very low values of GIC-index at low-mid latitudes, suggesting a greater participation of the ring current system. In any case, it is possible to observe the different impact of this storm at two different MLTs that is in good agreement with the reconstruction of the geomagnetic disturbance as recorded on the ground (see Figure 9).

6 Conclusions

The solar event occurred on August 20, 2018 has been capable to increase the intensity of the various electric current systems flowing in the magnetosphere and ionosphere activating a chain of processes which cover a wide range of time and spatial scales and, at the same time, to activate strong interactions between various regions within the solar-terrestrial system. The geomagnetic storm and the magnetospheric substorms occurred in the days following the solar event are the typical signatures of this chain of processes. The long lasting reconnection at the dayside magnetopause led to an increase of magnetospheric

420 circulation, to an injection of particles into the inner magnetosphere and more in general provided free energy which was stored in the magnetosphere and led to a worldwide magnetic disturbance. The development of such disturbance has led to an increase of currents in the ionosphere accompanied by the auroral activity and by a shift equatorward of the auroral electrojets and to the growth of the ring current (i.e. the westward toroidal electric current flowing around the Earth on the equatorial plane) accompanied by a worldwide reduction of the horizontal components of the geomagnetic field at low- and mid-latitudes. Rapid

425 geomagnetic variations induced geoelectric fields on the conducting ground responsible for GICs whose intensity, as expected, varied with geomagnetic latitude (*Tozzi et al.*, 2018, and references therein). The amplitude of these currents, quantified by means of the GIC index has reached values corresponding to "high" and "extreme" risk levels above $60°$ N of geomagnetic latitude. However, no failures or malfunctioning are reported in literature. A higher sampling of the different geomagnetic latitudes would have allowed to more precisely depict GIC variations with latitude.

430 This storm is one of the few strong geomagnetic storms (G3-class, https://spaceweather.com/) that occurred during the current, 24th, solar cycle and represents one of those cases which have clearly shown how unpredictable space weather is and how much work is needed to make reliable predictions of the effects that solar events could have on the terrestrial environment. Indeed, the CME emitted by the Sun in the days before the occurrence of the geomagnetic storm showed no features that would suggest the occurrence of important effects in the circumterrestrial environment or at ground. Indeed, as numerous studied have

435 shown, the magnitude and features of geomagnetic storms depend not only on solar wind plasma parameters and on the values of the IMF, but also on their evolution (*Piersanti et al.*, 2017, and references therein). Failing to predict the intensity of the August 26, 2018 storm has meant not being able to estimate correctly its effects on anthropic systems such as satellites, telecommunications, power transmission lines and the safety of airline passengers. This confirms that, despite considerable advances in understanding the drivers of space weather events, there is still room for improvements of their forecasting. It is

440 important to underline that the future capabilities of forecasting if, where and when an event occurs and how intense it will be, will depend on our understanding of the physical processes behind the dynamics in the near-Earth space (*Singer et al.*, 1998; *Pulkkinen*, 2015; *Piersanti and Carter*, 2019).

As a closing remark, we stress that, from a space weather point of view, this kind of comprehensive analysis plays a key role to better understand the complexity of the processes occurring in the Sun-Earth system that determines the geoeffectiveness of

445 solar activity manifestations.

Appendix A: RODI calculation

To define RODI it is necessary to calculate the rate of change of the electron density (ROD), defined as:

$$\text{ROD}(t) = \frac{Ne(t + \delta t) - Ne(t)}{\delta t}, \tag{A1}$$

where $Ne(t)$ and $Ne(t + \delta t)$ are the electron density measured by the Langmuir Probe on board the CSES satellite at time

450 t and $(t + \delta t)$, respectively; δt = 3 s since the CSES Langmuir Probe sampling rate is 1/3 Hz. Electron density values are

provided in the form of continuous time series as a function of time; however, missing measurements are possible, an issue that has to be taken into account from a computational point of view. Consequently, time and electron density measured values are indexed through an index k running on the whole time series. With this approach, the kth ROD value is calculated as:

$$\text{ROD}_k = \frac{Ne_{k+1} - Ne_k}{t_{k+1} - t_k},\tag{A2}$$

455   where Ne_k is the electron density measured at a specific time t_k and Ne_{k+1} is the electron density measured at time t_{k+1}, only when the condition $(t_{k+1} - t_k) = \delta t = 3$ s is satisfied, i.e. for time consecutive measurements (according to the Langmuir Probe sampling rate). RODI is the standard deviation of ROD values in a running window of Δt. Specifically, to calculate RODI, only ROD values calculated between $(t - \frac{\Delta t}{2})$ and $(t + \frac{\Delta t}{2})$ are taken into account. Then, RODI at each definite time t is:

$$\text{ROD}(t) = \sqrt{\frac{1}{N-1} \sum_{t_i = t - \frac{\Delta t}{2}}^{t + \frac{\Delta t}{2}} \left| \text{ROD}(t_i) - \overline{\text{ROD}}(t) \right|^2};\tag{A3}$$

     $\text{ROD}(t_i)$ are ROD values falling inside the window centered at time t and $\Delta t = 30$ s wide. N is the number of ROD values in the window, while $\overline{\text{ROD}}(t)$ is the corresponding mean, that is:

$$\overline{\text{ROD}}(t) = \frac{1}{N} \sum_{t_i = t - \frac{\Delta t}{2}}^{t + \frac{\Delta t}{2}} \text{ROD}(t_i).\tag{A4}$$

     From a computational point of view the kth RODI value is calculated as:

$$\text{RODI}_k = \sqrt{\frac{1}{N-1} \sum_{i=-j}^{j} \left| \text{ROD}_{k+i} - \overline{\text{ROD}}_k \right|^2},\tag{A5}$$

     where ROD_{k+i} are ROD values falling inside the window of width $(2j + 1)$, with $j = 5$, centered at the index k. To take into account possible missing measurements in the time series, only ROD values satisfying the condition $|t_{k+i} - t_k| \leq \frac{\Delta t}{2} = 15$ s are considered. N is the number of ROD values (at most 11) falling in the window, and $\overline{\text{ROD}}_k$ is the corresponding mean of these N values, that is:

$$\overline{\text{ROD}}_k = \frac{1}{N} \sum_{i=-j}^{j} \text{ROD}_{k+i}.\tag{A6}$$

     Finally, RODI is calculated only when at least 6 ROD values fall in the window (the half plus one of maximum values inside a window, with $\delta t = 3$ s and $\Delta t = 30$ s). In this way, windows poorly populated, and consequently not statistically reliable, are discarded.

Author contributions. MP managed the manuscript, made the analysis the magnetic field data from both satellite and ground observations, and concurred to the discussion of the results; PDM analyzed the geomagnetic data and concurred to the discussion of the results; RT made the GIC analysis and concurred to the discussion of the results; DDM analyzed Solar data and run the simulation of the ICME propagation; MP and AP analyzed the ionospheric plasma data and evaluated both ROTI and RODI; GC and VQ analyzed the magnetospheric field data and concurred to the discussion of the results; SDM analyzed the Solar Wind data; PD validate and processed the CSES data; ML made the interplanetary analysis; MFM made the magnetospheric analysis; all the authors approved the final version of the manuscript.

Competing interests. The Author's declare that no competing interest are present.

Acknowledgements. The results presented in this paper rely on data collected at magnetic observatories. SDO Data is courtesy of NASA SDO/AIA and the HMI science teams. SOHO Data supplied courtesy of the SOHO/MDI and SOHO/EIT consortia. SOHO is a project of international cooperation between ESA and NASA. This research has made use of data provided by the Heliophysics Event Knowledgebase. DSCOVR data were obtained from the NOAA's National Centers for Environmental Information (NCEI) Data Center. We thank the national institutes that support them and INTERMAGNET for promoting high standards of magnetic observatory practice (www.intermagnet.org). This work made use of the data from CSES mission (http://www.leos.ac.cn/), a project funded by China National Space Administration and China Earthquake Administration in collaboration with Italian Space Agency and Istituto Nazionale di Fisica Nucleare. The authors kindly acknowledge N. Papitashvili and J. King at the National Space Science Data Center of the Goddard Space Flight Center for the use permission of 1-minute OMNI data and the NASA CDAWeb team for making these data available. We acknowledge use of NOAA Space Weather Prediction Center for obtaining GOES magnetometer data. The European Space Agency (ESA) is acknowledged for providing the Swarm data. The official Swarm website is http://earth.esa.int/swarm. M. Piersanti thanks the Italian Space Agency for the financial support under the contract ASI "LIMADOU scienza" n° 2016-16-H0. This research work is supported by the Italian MIUR-PRIN on *Circumterrestrial environment: impact of Sun - Earth interaction.*

References

495   Alberti, T., G. Consolini, F. Lepreti et al., (2017), Timescale separation in the solar wind-magnetosphere coupling during St. Patrick's Day storms in 2013 and 2015, *J. Geophys. Res.*, 122, 4266–4283, https://doi.org/10.1002/2016JA023175.

Alberti, T., G. Consolini, P. De Michelis et al., (2018), On fast and slow Earth's magnetospheric dynamics during geomagnetic storms: a stochastic Langevin approach, *J. Space Weather Space Clim.*, 8, A56, https://doi.org/10.1051/swsc/2018039.

Baker D.N., (2001), Satellite Anomalies due to Space Storms. In: Daglis I.A. (eds) *Space Storms and Space Weather Hazards*. NATO Science

500   Series (Series II: Mathematics, Physics and Chemistry), vol 38. Springer, Dordrecht, https://doi.org/10.1007/978-94-010-0983-6_11.

Baker, K. B., and S. Wing, (1989), A new magnetic coordinate system for conjugate studies at high latitudes, *J. Geophys. Res.*, 94, A7, 9139, https://doi.org/10.1029/JA094iA07p09139.

Bothmer, V., and R. Schwenn, (1995), The interplanetary and solar causes of major geomagnetic storms, *J. Geomagn. Geoelectr.*, 47, 1127, https://doi.org/10.5636/jgg.47.1127.

505   Brueckner, G.E., R. A. Howard, M. J. Koomen, C. M. Korendyke, D. J. Michels,J. D. Moses, D. G. Socker, K. P. Dere, P. L. Lamy, A. Llebaria and M. V. Bout, (1995), The large angle spectroscopic coronagraph (LASCO), *Sol. Phys.*, 162, 357, https://doi.org/10.1007/BF00733434.

Burlaga, L., Sittler, E., Mariani, F., and Schwenn, a. R. (1981), Magnetic loop behind an interplanetary shock: Voyager, helios, and imp 8 observations. *J. Geophys. Res.*, 86(A8), 6673.

Burt, J. and B. Smith, (2012), Deep Space Climate Observatory: The DSCOVR mission, *Aerospace Conference 2012 IEEE*, Aerospace

510   Conference, IEEE, 1, https://doi.org/10.1109/AERO.2012.6187025.

Carter, B. A., E. Yizengaw, R. Pradipta, J. M. Weygand, M. Piersanti, A. Pulkkinen, M. B. Moldwin, R. Norman, and K. Zhang, (2016), Geomagnetically induced currents around the world during the 17 march 2015 storm, *J. Geophys. Res.*, 121, 10,496, 507, https://doi.org/2016JA023344.

Chisham, G. M. Lester,S. Milan, M. Freeman, W. Bristow, W., A. Grocott, K. McWilliams, J. Ruohoniemi, J. T. Yeoman, Timothy,

515   P. Dyson, R. Greenwald, T. Kikuchi, M. Pinnock, J.Rash, N. Sato, G. Sofko, J.-P Villain, J.-P and A. Walker,(2007), A decade of the Super Dual Auroral Radar Network (SuperDARN): Scientific achievements, new techniques and future directions, *Surv. Geophys.*28,https://doi.org/10.1007/s10712-007-9017-8.

Consolini, G., M.F. Marcucci, and M. Candidi, (1996), Multifractal Structure of Auroral Electrojet Index Data, *Phys. Rev. Lett.*, 76, 4082–4085.

520   Consolini, G., (1997), Sandpile Cellular Automata and Magnetospheric Dynamics, *Proc. of "VIII Conv. GIFCO-97*, S. Aiello et al. eds., SIF (Bo), 127.

Consolini, G., and P. De Michelis, (1998), Non-Gaussian Distribution Function of AE-Index Fluctuations. Evidence for Time Intermittency, *Geophys. Res. Lett.*, 25, 4087-4090.

Consolini, G., (2002), Self-organized criticality: a new paradigm for the magnetotail dynamics, *Fractals*, 10, 275.

525   Consolini, G., and P. De Michelis, (2005), Local intermittency measure analysis of AE index: The directly driven and unloading component, *Geophys. Res. Lett.*, 32, L05101, https://doi.org/10.1029/2004GL022063.

Consolini, G., T. Alberti, and P. De Michelis, (2018), On the Forecast Horizon of Magnetospheric Dynamics: A Scale-to-Scale Approach, *J. Geophys. Res.*, 123, 9065–9077, https://doi.org/10.1029/2018JA025952.

Del Moro, D., G. Napoletano, A. Cristaldi, R. Forte, L. Giovannelli, E. Pietropaolo, and F. Berrilli, (2019), Forecasting the 2018 February

530   12th CME propagation with the P-DBM model: a fast warning procedure, *Ann. Geophys.*, 61, https://doi.org/10.4401/ag-7750.

De Michelis, P., I. Daglis and G. Consolini, (1997), Average terrestrial ring current derived from AMPTE/CCE-CHEM measurements, *J. Geophys. Res.*, 102, 14103, https://doi.org/10.1029/96JA03743.

De Michelis, P., I. Daglis, and G. Consolini, (1999), An average image of proton plasma pressure and of current systems in the equatorial plane derived from AMPTE/CCE-CHEM measurements, *J. Geophys. Res.*, 104, 28615, https://doi.org/10.1029/1999JA900310.

535 De Michelis, P, G. Consolini, R. Tozzi, M.F. Marcucci, (2016), Observations of high-latitude geomagnetic field fluctuations during St. Patrick's Day storm: Swarm and SuperDARN measurements, *Earth, Planets Space*, 68:105, 1-16, https://doi.org/10.1186/s40623-016-0476-3.

Domingo, V., B. Fleck and A. I. Poland, (1995). The SOHO mission: an overview, *Solar Physics*, 162 (1-2), pp. 1, https://doi.org/10.1007/BF00733425.

540 Finlay, C. C., N. Olsen, S. Kotsiaros, N. Gillet and L. Toffer-Clausen, (2016), Recent geomagnetic secular variation from Swarm and ground observatories as estimated in the CHAOS-6 geomagnetic field model, *Earth Planet Space*, 68, 112, https://doi.org/10.1186/s40623-016-0486-1.

Fox, N. J., M. C. Velli, S. D. Bale, R. Decker, A. Driesman, R. A. Howard, Justin C. Kasper, J. Kinnison, M. Kusterer, D. Lario, M. K. Lockwood, D. J. McComas,N. E. Raouafi and A. Szabo, (2016), The Solar Probe Plus mission: Humanity's first visit to our star, *Space*
545 *Science Reviews*, 204, 1-4, 7, https://doi.org/ 10.1007/s11214-015-0211-6.

Friis-Christensen, E., H. Lühr and G. Hulot, (2006), Swarm: A constellation to study the Earth's magnetic field, *Earth Planets Space* 58, 351, https://doi.org/10.1186/BF03351933.

Friis-Christensen, E., H. Lühr, D. Knudsen and R. Haagmans, (2008), Swarm – An Earth Observation Mission investigating Geospace, *Advances Space Research* 41, 1, 210, https://doi.org/10.1016/j.asr.2006.10.008.

550 Ganushkina, N. Y., M. W. Liemohn, and S. Dubyagin (2018), Current systems in the Earth's magnetosphere, *Rev. Geophys.*, 56, 309, https://doi.org/10.1002/2017RG000590.

Ginet, G. P., (2001), Space Weather: An Air Force Research Laboratory Perspective. In: Daglis I.A. (eds), *Space Storms and Space Weather Hazards*, NATO Science Series (Series II: Mathematics, Physics and Chemistry), vol 38. Springer, Dordrecht, https://doi.org/10.1007/978-94-010-0983-6_18.

555 Gonzalez, W. D., and B. T. Tsurutani, (1987), Criteria of interplanetary parameters causing intense magnetic storms (Dst < -100nT), *Planet. Space Sci.*, 35, 1101, https://doi.org/10.1016/0032-0633(87)90015-8.

Gonzalez, W. D., J. A. Joselyn, Y. Kamide, H. W. Kroehl, G. Rostoker, B. T. Tsurutani, and V. M. Vasyliunas (1994), What is a geomagnetic storm?, *J. Geophys. Res.*, 99 (A4), 5771, https://doi.org/10.1029/93JA02867.

Gosling, J. T. (1993), The solar flare myth, *J. Geophys. Res.*, 98, (A11), 18937, https://doi.org/10.1029/93JA01896.

560 Hapgood, M. (2019), The Great Storm of May 1921: An Exemplar of a Dangerous Space Weather Event, *Space Weather*, 17(7), 950–975, doi:10.1029/2019SW002195.

Hargreaves, J., (1992), The Solar-Terrestrial Environment: An Introduction to Geospace - the Science of the Terrestrial Upper Atmosphere, Ionosphere, and Magnetosphere, *Cambridge Atmospheric and Space Science Series*, Cambridge: Cambridge University Press, https://doi.org/10.1017/CBO9780511628924.

565 Howard, R.A., J. D. Moses, A. Vourlidas, J. S. Newmark, D. G. Socker, S. P. Plunkett, C. M. Korendyke, J. W. Cook, A. Hurley, J. M. Davila, and W. T. Thompson, (2008), Sun Earth connection coronal and heliospheric investigation (SECCHI), *Space Science Reviews*, 136, (1-4), 67, https://doi.org/10.1016/S0273-1177(02)00147-3.

Howard, T. A., and R. A. Harrison, (2013), Stealth coronal mass ejections: A perspective, *Solar Physics*, 285, 1-2 269, https://doi.org/10.1007/s11207-012-0217-0.

570 Iyemori, T. (1990), Storm-time magnetospheric currents inferred from mid–latitude geomagnetic field variations, J. Geomagn. Geoelec., 42 (11), 1249-1265, doi:10.5636/jgg.42.1249.

Isavnin, A., A. Vourlidas, and E. K. J. Kilpua, (2013), Three-Dimensional Evolution of Flux-Rope CMEs and Its Relation to the Local Orientation of the Heliospheric Current Sheet, *Solar Physics*, 289, 2141, https://doi.org/10.1007/s11207-013-0468-4.

Jakosky, B. M., R. P. Lin, J. M. Grebowsky, J. G. Luhmann, D. F. Mitchell, G. Beutelschies, T. Priser et al., (2015), The Mars atmosphere
575 and volatile evolution (MAVEN) mission, *Space Science Reviews* 195, 1-4, 3, https://doi.org/10.1007/s11214-015-0139-x.

Jin, Y. and K. Oksavik, (2018), GPS scintillations and losses of signal lock at high latitudes during the 2015 St. Patrick's Day storm, *J. Geophys. Res.*, 123, https://doi.org/10.1029/2018JA025933.

Kaiser, M.L., T. A. Kucera, J. M. Davila, O. S. Cyr, M. Guhathakurta and E. Christian, (2008), The STEREO mission: An introduction, *Space Science Reviews*, 136, 1-4, 5, https://doi.org/10.1007/s11214-007-9277-0.

580 Kappenman, J. G., (2001), An Introduction to Power Grid Impacts and Vulnerabilities from Space Weather, in: Daglis I.A. (eds), *Space Storms and Space Weather Hazards*, NATO Science Series (Series II: Mathematics, Physics and Chemistry), 38, Springer, Dordrecht, https://doi.org/10.1007/978-94-010-0983-6_13.

Koskinen, H. E. J., D. N. Baker, A. Balogh, T. Gombosi, A. Veronig, R. von Steiger, (2017), Achievements and Challenges in the Science of Space Weather, *Space Science Review*, 212, 1137, https://doi.org/10.1007/s11214-017-0390-4.

585 Lanzerotti, L.J., (2001), Space Weather Effects on Communications, in: Daglis I.A. (eds), *Space Storms and Space Weather Hazards*, NATO Science Series (Series II: Mathematics, Physics and Chemistry), 38, Springer, Dordrecht, https://doi.org/10.1007/978-94-010-0983-6_12.

Lemen, J.R., D. J. Akin, P. F. Boerner, C. Chou, J. F. Drake, D. W. Duncan, C. G. Edwards, F. M. Friedlaender, G. F. Heyman, N. E. Hurlburt and N. L. Katz, (2011). The atmospheric imaging assembly (AIA) on the solar dynamics observatory (SDO), *In The solar dynamics observatory*, 17, Springer, New York, NY, https://doi.org/10.1007/s11207-011-9776-8.

590 Lepping, R.P., M. H., Acuña, L. F. Burlaga, W. M. Farrell, J. A. Slavin, K. H. Schatten, F. Mariani, N. F. Ness, F. M. Neubauer, Y. C. Whang, J. B. Byrnes, R. S. Kennon, P. V. Panetta, J. Scheifele and E. M. Worley, (1995), The WIND magnetic field investigation, *Space. Sci. Rev.*, 71, 207 https://doi.org/10.1007/BF00751330.

Lui, A.T.Y., S.C. Chapman, K. Liou, et al., (2000), Is the dynamic magnetosphere an avalanching system ?, *Geophys. Res. Lett.*, 27, 911-914.

Marshall, R. A., C. L. Waters and M. D. Sciffer, (2010), Spectral analysis of pipe-to-spoil potentials with variations of the Earth's magnetic
595 field in the Australian region, *Space Weather*, 8, S05002, https://doi.org/ 10.1029/2009SW000553.

Marshall, R. A., E. A. Smith, M. J. Francis, C. L. Waters and M. D. Sciffer, (2011), A preliminary risk assessment of the Australian region power network to space weather, *Space Weather*, 9, S10004, https://doi.org/10.1029/2011SW000685.

McPherron, R. L., (1995), Magnetospheric dynamics, *Introduction to Space Physics*, eds M. G. Kivelson and C. T. Russell, Cambridge University Press.

600 Menvielle, M., T. Iyemori, A. Marchaudon, and M. Nosé, (2011), Geomagnetic Indices, in M. Mandea, M. Korte (eds.), in *Geomagnetic Observations and Models*, IAGA Special Sopron Book Series 5, 183, Springer Science+Business Media B.V., https://doi.org/10.1007/978-90-481-9858-0_8,

Milan S.E, L.B.N. Clausen, J.C. Coxon, J.A. Carter, M.-T. Walach, K. Laundal, N. Østgaard, P. Tenfjord, J. Reistad, K. Snekvik, H. Korth, B.J. Anderson, Overview of Solar Wind–Magnetosphere–Ionosphere–Atmosphere Coupling and the Generation of Magnetospheric Currents,
605 *Space Sci Rev*, 206, https://doi.org/10.1007/s11214-017-0333-0.

Moon, Y. J., G. S. Choe, H. Wang, Y. D. Park, N. Gopalswamy, G. Yang, and S. Yashiro, (2002), A statistical study of two classes of coronal mass ejections. *The Astrophysical Journal*, 581, 1, 694, https://doi.org/10.1086/344088.

Napoletano, G., R. Forte, D. Del Moro, E. Pietropaolo, L. Giovannelli and F. Berrilli (2018), A probabilistic approach to the drag-based model, *J. Space Weather Space Clim.*, 8, A11, https://doi.org/10.1051/swsc/2018003.

610   Nishitani N., Ruohoniemi J.M., Lester M., Baker J.B.H., Koustov A.V., Shepherd S.G., Chisham G., Hori T., Thomas E.G., Makarevich R.A., Marchaudon A., Ponomarenko P., Wild J., Milan S., Bristow W.A., Devlin J., Miller E., Greenwald R.A., Ogawa T., Kikuchi T., (2019), Review of the accomplishments of midlatitude Super Dual Auroral Radar Network (SuperDARN) HF radars, *Prog Earth Planet Sci 6* 27, https://doi.org/10.1186/s40645-019-0270-5.

Prog Earth Planet Sci 6, 27 (2019) doi:10.1186/s40645-019-0270-5

615   Pesnell, W. D., B. J. Thompson, and P. C. Chamberlin, (2011), The solar dynamics observatory (SDO), *In The Solar Dynamics Observatory*, pp. 3-15. Springer, New York, NY, https://doi.org/10.1007/s11207-011-9841-3.

Pezzopane, M., A. Del Corpo, M. Piersanti, C. Cesaroni, A. Pignalberi, S. Di Matteo, L. Spogli, M. Vellante and B. Heilig, (2019), On some features characterizing the plasmasphere–magnetosphere–ionosphere system during the geomagnetic storm of 27 May 2017, *Earth Planets Space*, 71, 77, https://doi.org/10.1186/s40623-019-1056-0.

620   Piersanti, M., U. Villante, C. Waters, and I. Coco (2012), The 8 June 2000 ULF wave activity: A case study, *J. Geophys. Res.*, 117, A02204, https://doi.org/10.1029/2011JA016857.

Piersanti, M., and U. Villante (2016), On the discrimination between magnetospheric and ionospheric contributions on the ground manifestation of sudden impulses, *J. Geophys. Res-Space*, *121*(7), 6674, https://doi.org/10.1002/2015JA021666.

Piersanti, M., T. Alberti, A. Bemporad, F. Berrilli, R. Bruno, V. Capparelli, V. Carbone, C. Cesaroni, G. Consolini, A. Cristaldi, A. Del Corpo,

625   D. Del Moro, S. Di Matteo, I. Ermolli, S. Fineschi, F. Giannattasio, F. Giorgi, L. Giovannelli, S. L. Guglielmino, M. Laurenza, F. Lepreti, M. F. Marcucci, M. Martucci, M. Mergè, M. Pezzopane, E. Pietropaolo, P. Romano, R. Sparvoli, L. Spogli, M. Stangalini, A. Vecchio, M. Vellante, U. Villante, F. Zuccarello, B. Heilig, J. Reda, and J. Lichtenberger (2017a), Comprehensive analysis of the geoeffective solar event of 21 june 2015: Effects on the magnetosphere, plasmasphere, and ionosphere systems, *Solar Physics*, 292, (11), 169, https://doi.org/10.1007/s11207-017-1186-0.

630   Piersanti, M., M. Materassi, A. Cicone, L. Spogli, H. Zhou and R. G. Ezquer (2018), Adaptive local iterative filtering: A promising technique for the analysis of nonstationary signals, *J. Geophys. Res.*, 123, (1), 1031, https://doi.org/10.1002/2017JA024153.

Piersanti, M. and B. A. Carter, (2019), Geomagnetically induced currents, in *The Dynamical Ionosphere. A Systems Approach to Ionospheric Irregularity*, M. Materassi, B. Forte, A. Coster, S. Skone (eds), Elsevier, ISBN: 9780128147825.

Piersanti, M., S. Di Matteo, B. A. Carter, J. Currie and G. D'Angelo (2019). Geoelectric field evaluation during the September 2017 Geo-

635   magnetic Storm: MA.I.GIC. model, *Space Weather*, 17, 1241, https://doi.org/10.1029/2019SW002202.

Pignalberi, A., M. Pezzopane, R. Tozzi, P. Michelis, and I. Coco (2016), Comparison between IRI and preliminary Swarm Langmuir probe measurements during the St. Patrick storm period, *Earth, Planets Space* 68, 93, https://doi.org/10.1186/s40623-016-0466-5.

Pilipenko, V. A., M. Bravo, N. V. Romanova, O. V. Kozyreva, S. N. Samsonov, Ya. A. Sakharov, (2018), Geomagnetic and Ionospheric Responses to the Interplanetary Shock Wave of March 17, 2015, Izv., *Phys. Solid Earth*, 54, 721,

640   https://doi.org/10.1134/S1069351318050129.

Pulkkinen, A. (2015), Geomagnetically Induced Currents Modeling and Forecasting, *Space Weather*, 13, 734, https://doi.org/10.1002/2015SW001316.

Pulkkinen, A., E. Bernabeu, A. Thomson, A. Viljanen, R. Pirjola, D. Boteler, J. Eichner, P. J. Cilliers, D. Welling, N. P. Savani, R. S. Weigel, J. J. Love, C. Balch, C. M. Ngwira, G. Crowley, A. Schultz, R. Kataoka, B. Anderson, D. Fugate, J. J. Simpson, M. MacAlester, (2017), Geomagnetically induced currents: Science, engineering, and applications readiness, *Space Weather*, 15, 828–856, https://doi.org/doi:10.1002/2016SW001501.

Richardson, I. G., (2018), Solar wind stream interaction regions throughout the heliosphere, *Living reviews in solar physics*, 15, 1, 1, https://doi.org/10.1007/s41116-017-0011-z.

Rishbeth, J.A. and Garriot O.K., (1969), Introduction to Ionospheric Physics, *New York*: Academic Press.

Stone, E. C., A. M. Frandsen, R. A. Mewaldt, E. R. Christian, D. Margolies, J. F. Ormes, and F. Snow, (1998), The advanced composition explorer, *Space Science Reviews*, 86, 1, 1, https://doi.org/10.1023/A:1005082526237.

Szabo, A. (1994), An improved solution to the "rankine-hugoniot" problem, *J. Geophys. Res.*, 99, (A8), 14,737, 746, https://doi.org/10.1029/94JA00782.

Shen, C., Y. Chi, Y. Wang, M. Xu, and S. Wang, (2017), Statistical comparison of the ICME's geoeffectiveness of different types and different solar phases from 1995 to 2014, *J. Geophys. Res.*, 122, (6), 5931, https://doi.org/10.1002/2016JA023768.

Shen, X., Q. Zong, and X. Zhang, (2018), Introduction to special section on the China Seismo-Electromagnetic Satellite and initial results. *Earth Planetary Phys.*, 2, 439, https://doi.org/10.26464/epp2018041.

Shue, J.-H., P. Song, C. T. Russell, J. T. Steinberg, J. K. Chao, G. Zastenker, O. L. Vaisberg, S. Kokubun, H. J. Singer, T. R. Detman, H. Kawano, (1998), Magnetopause location under extreme solar wind conditions, *J. Geophys. Res.*, 103 (A8), 17691, https://doi.org/10.1029/98JA01103.

Singer, H., G. Heckman and J. Hirman, (2013), Space Weather Forecasting: A Grand Challenge. In *Space Weather*, P. Song, H. J. Singer and G. L. Siscoe (eds.), https://doi.org/10.1029/GM125p0023.

Sitnov, M.I., A.S. Sharma, K. Papadopoulos, et al., (2001), Modeling substorm dynamics of the magnetosphere: From self-organization and self-organized criticality to nonequilibrium phase transitions, *Phys. Rev. E*, 65, 016116.

Smith, E.J., B. T. Tsurutani and R. L. Rosenberg, (1978), Observations of the interplanetary sector structure up to heliographic latitudes of 16°: pioneer 11. *J. Geophys. Res.*, 83, 717, https://doi.org/10.1029/JA083iA02p00717.

Smith, A. R. A., C. D. Beggan, S. Macmillan, and K. A. Whaler, (2017), Climatology of the auroral electrojets derived from the along-track gradient of magnetic field intensity measured by POGO, Magsat, CHAMP, and Swarm, *Space Weather*, 15, 1257, https://doi.org/10.1002/2017SW001675.

Souza, V. M., D. Koga, W. D. Gonzalez, and F. R. Cardoso, (2017), Observational aspects of magnetic reconnection at the earth's magnetosphere, *Brazilian Journal of Physics*, 47 (4), 447, https://doi.org/10.1007/s13538-017-0514-z.

Thomas, E. G., and Shepherd, S. G. (2018), Statistical patterns of ionospheric convection derived from mid-latitude, high-latitude, and polar SuperDARN HF radar observations, *J. Geophys. Res.*, 123, 3196–3216. https://doi.org/10.1002/2018JA025280

Tozzi, R., I. Coco, P. De Michelis and F. Giannattasio, (2018), Latitudinal dependence of geomagnetically induced currents during geomagnetic storms, *Annals of Geophysics*, 61, https://doi.org/10.4401/ag-7788.

Tozzi, R., P. De Michelis, I. Coco, and F. Giannattasio, (2019), A Preliminary Risk Assessment of Geomagnetically Induced Currents over the Italian Territory, *Space Weather*, 17, 46, https://doi.org/10.1029/2018SW002065.

Tsurutani, B.T., W. D. Gonzalez, F. Tang, S. I. Akasofu and E. J. Smith, (1988), Origin of interplanetary southward magnetic fields responsible for major magnetic storms near solar maximum (1978 – 1979). *J. Geophys. Res.* 93 (A8), 8519. https://doi.org/10.1029/JA093iA08p08519.

680 Tsyganenko, N. A., and M. I. Sitnov (2005), Modeling the dynamics of the inner magnetosphere during strong geomagnetic storms, *J. Geophys. Res.*, 110 (A3), https://doi.org/10.1029/2004JA010798.

Uritsky, V.M., and M. I. Pudovkin (1998), Low frequency 1/f-like fluctuations of the AE-index as a possible manifestation of self-organized criticality in the magnetosphere, *Ann. Geophys.*, 16, 1580-1588.

Uritsky, V.M., A.J. Klimas, D. Vasiliadis, et al., (2002), Scale-free statistics of spatiotemporal auroral emissions as depicted by POLAR UVI
685 images: Dynamic magnetosphere is an avalanching system, *J. Geophys. Res.*, 107, 1426, https://doi.org/10.1029/2001JA000281.

Villante U., M. Piersanti, Sudden impulses at geosynchronous orbit and at ground, (2011), *J. Atm. Sol. Terr. Phys.*, 73, 1, 61, https://doi.org/10.1016/j.jastp.2010.01.008.

Viñas, A. F., and J. D. Scudder (1986), Fast and optimal solution to the "rankine-hugoniot problem", *J. Geophys. Res.*, 91, (A1), 39, https://doi.org/10.1029/JA091iA01p00039.

690 Vrsnak, B., T. Zic, D. Vrbanec, M. Temmer, T. Rollett, C. Mostl, A. Veronig, J. Calogovic, M. Dumbovic, S. Lulic, Y. J. Moon and A. Shanmugaraju (2013), Propagation of interplanetary coronal mass ejections: the drag-based model, *Solar physics*, 285, 1-2, 295, https://doi.org/10.1007/s11207-012-0035-4.

Wang, C., H. Li, J. D. Richardson, and J. R. Kan, (2010), Interplanetary shock characteristics and associated geosynchronous magnetic field variations estimated from sudden impulses observed on the ground, *J. Geophys. Res.*, 115, A09215,https://doi.org/10.1029/2009JA014833.

695 Wang X., W. Cheng, D. Yang and D. Liu, (2019), Preliminary validation of in situ electron density measurements onboard CSES using observations from Swarm Satellites, *Adv. Sp. Res.* 64, 982, https://doi.org/10.1016/j.asr.2019.05.025.

Yurchyshyn, V., S. Yashiro, V. Abramenko, H. Wang and N. Gopalswamy (2005), Statistical distributions of speeds of coronal mass ejections, *The Astrophysical Journal*, 619 (1), 599, https://doi.org/10.1086/426129.

Zhou, B., B. Cheng, X. Gou, L. Li, Y. Zhang, J. Wang, W. Magnes, R. Lammegger, A. Pollinger, M. Ellmeier, Q. Xiao, X. Zhu, S. Yuan, Y.
700 Yang and X. Shen, (2019), First in-orbit results of the vector magnetic field measurement of the High Precision Magnetometer onboard the China Seismo-Electromagnetic Satellite, *Earth Planets Space*, 71, 119, https://doi.org/10.1186/s40623-019-1098-3.

Zurbuchen, T.H. and I. G. Richardson, (2006), In-Situ Solar Wind and Magnetic Field Signatures of Interplanetary Coronal Mass Ejections. In: Coronal Mass Ejections. *Space Sciences Series of ISSI*, 21, Springer, New York, NY, https://doi.org/10.1007/978-0-387-45088-9-3.
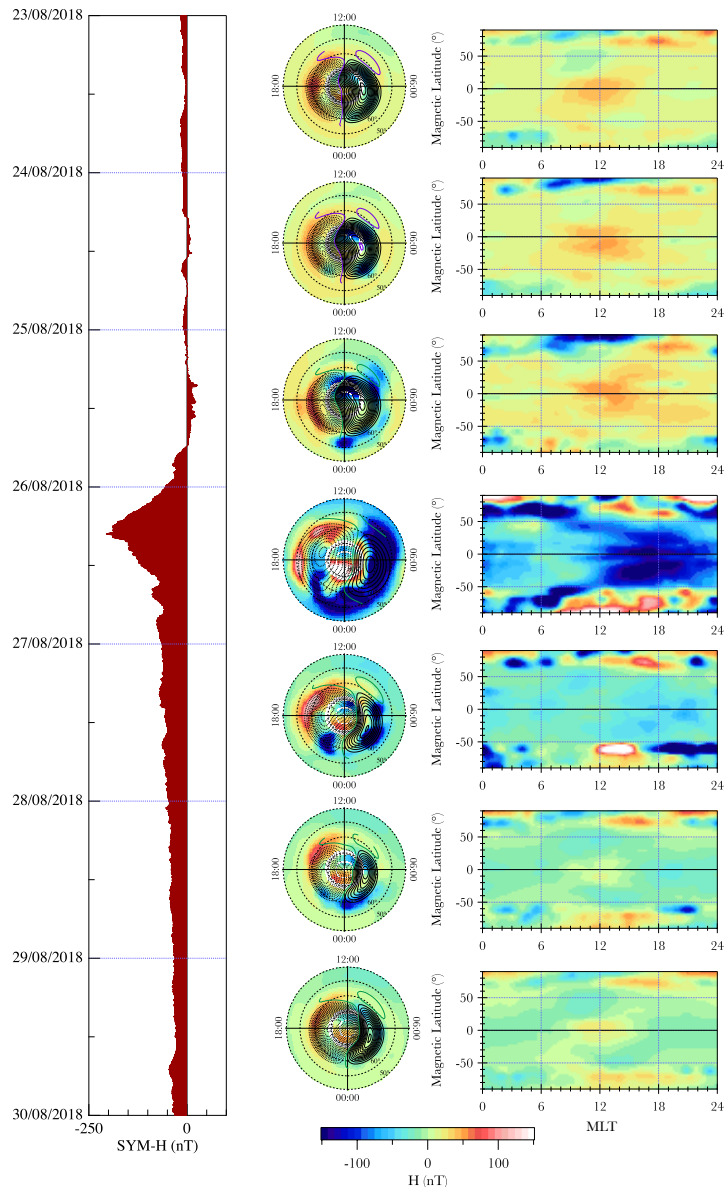
Figure 9. On the left the evolution of the SYM-H index; in the middle column, daily polar view maps of the horizontal field magnitude in the Northern Hemisphere. The convection patterns derived from the SuperDARN based model of (*Thomas and Shepherd*, 2018) are over plotted on the horizontal field magnitude; on the right column the worldwide view of the same magnetic field component. Data are reported in geomagnetic latitude and MLT, referring to a period of seven days from August 23, 2018 to August 29, 2018.
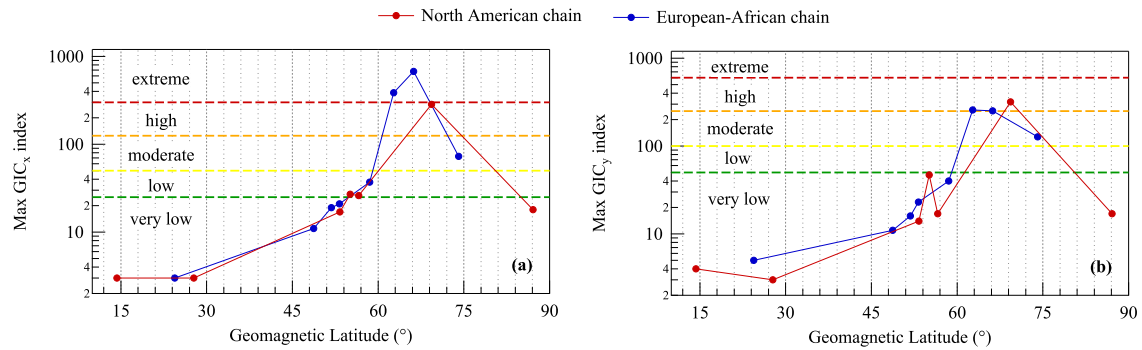
Figure 10. Maximum value of the GIC indices, occurred in the time interval from August 25, 2018 at 18:00 UT August 26, 2018 at 18:00 UT, as observed at the magnetic observatories of both the North American and European-African latitudinal chain. In detail, panel a) displays the maximum values of the GIC_x index, panel b) the maximum values of the GIC_y index. Colored dashed lines indicate the thresholds between the different risk levels as defined by *Marshall et al.* (2011).
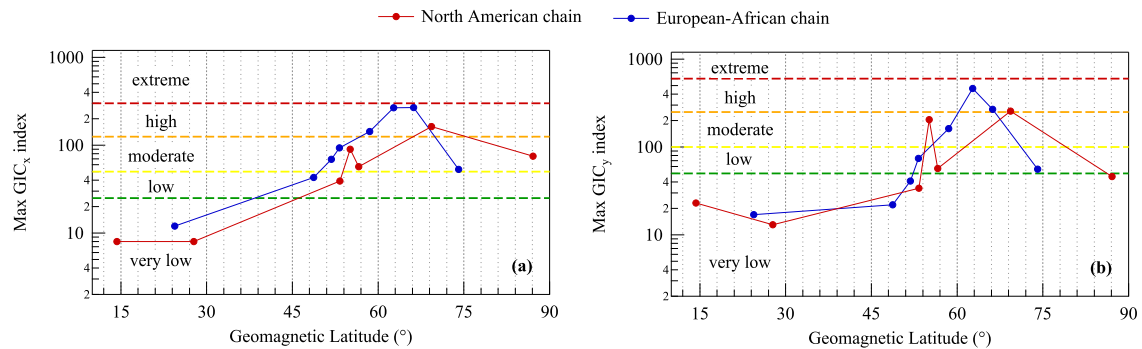
Figure 11. Maximum value of the GIC indices, occurred in the time interval from March 17, 2015 at 04:00 UT to March 18, 2015 at 04:00 UT, as observed at the magnetic observatories of both the North American and European-African latitudinal chain. In detail, panel a) displays the maximum values of the GIC_x index, panel b) the maximum values of the GIC_y index. Colored dashed lines indicate the thresholds between the different risk levels as defined by *Marshall et al.* (2011)